Supporting Information

Metal-ligand bond strength determines the fate of organic ligands on the catalyst surface during the electrochemical CO_2 reduction reaction

James R. Pankhurst,[a] Pranit Iyengar,[a] Anna Loiudice,[a] Mounir Mensi,[b] and Raffaella Buonsanti[a]*

[a] Laboratory of Nanochemistry for Energy (LNCE), Institute of Chemical Sciences and Engineering (ISIC), École Polytechnique Fédérale de Lausanne, 1950 Sion, Valais, Switzerland

[b] Institute of Chemical Sciences and Engineering (ISIC), École Polytechnique Fédérale de Lausanne, 1950 Sion, Valais, Switzerland

Table of Contents

Experimental Procedures

Materials

Copper(I) acetate (Cu(OAc), 98%), tri-*n*-octylamine (TOA, technical grade, 98%), oleylamine (OLAM, technical grade, 70%), oleic acid (OLAC, technical grade, 90%), tri-*n*-octylphosphine (TOP, technical grade, 90%), tri-*n*-octylphosphine oxide (TOPO, 99%), tetradecylphosphonic acid (TDPA, 97%), dodecanethiol (DDT, 98%), Meerwein's salt (specifically, $[Me_3O][BF_4]$, 95%), tetrabutylammonium hexafluorophosphate (>99%, electrochemical analysis grade), Chelex resin (100 sodium form, 50-100 mesh, dry), toluene (anhydrous, 99.8%), *N,N*-dimethylformamide (anhydrous, 99.8%), and ethanol (anhydrous, 95%) were purchased from Sigma Aldrich. K_2CO_3 (99.995%) was purchased from Roth AG. d_6-Benzene was purchased from ReseaChem GmbH (Cambridge Isotope Laboratories). Hexane (anhydrous, >96%) was purchased from TCI Deutschland GmbH, acetonitrile (anhydrous, 99.8%) was purchased from ABCR GmbH, and acetone (anhydrous, synthesis grade) was purchased from Fisher Chemical.

Prior to use, Chelex resin was activated with HCl and NaOH according to the details given below. d_6-Benzene was dried using 4 Å molecular sieves (Sigma Aldrich) and was degassed by sparging with N_2 before storing in a N_2-filled glove box. TOA, OLAM, OLAC, TOPO and DDT were degassed by stirring under dynamic vacuum before storing in a N_2-filled glove box.

Methods

General considerations. All syntheses and manipulations of CuNCs were done under a dry N_2 atmosphere, using Schlenk-line techniques or a glove box. Anhydrous organic solvents were used for the manipulation, analysis and storage of CuNCs. All volumes were measured and dispensed using Eppendorf microliter pipettes.

Inductively-coupled plasma optical emission spectroscopy (ICP-OES) measurements were carried out using an Agilent 5100 model to determine the Cu concentration in catalyst stock solutions. Five standard solutions of Cu were prepared to obtain calibration curves used to determine the concentrations of the digested nanocrystal solution. The sample solution was prepared by digesting the nanocrystals in 70% high-purity HNO_3; deionised water was then added to dilute the acid concentration to 2% for analysis.

Transmission electron microscopy (TEM) images were recorded using a FEI Tecnai-Spirit at 120 kV. Samples were prepared by dropping hexane solutions of the nanocrystals onto carbon-coated copper TEM grids (Ted Pella, Inc.). Size statistics were performed using ImageJ software by counting at least 100 NCs per sample.

Scanning electron microscopy (SEM) images were acquired on a FEI Teneo microscope using an inlens (Trinity) detector at a beam energy of 5 keV and a beam current of 0.4 nA. Energy Dispersive X-ray Analysis (EDX) was performed under the same conditions with an XFlash Silicon drift detector. Post-CO_2RR samples were studied directly on the glassy carbon electrodes.

Fourier transform infra-red spectroscopy (FT-IR) was carried out on a Perkin Elmer Two spectrometer using an attenuated total reflectance (ATR) plate. Air was used as a background spectrum. Samples were prepared by drop-casting hexane suspensions of the CuNCs directly onto the ATR plate and leaving to air-dry. Spectra were recorded with a resolution of 4 cm^{-1} and a total of 16 scans.

UV-vis absorption spectra were recorded in transmission mode using a Perkin Elmer Lambda 950 spectrophotometer equipped with a tungsten halide lamp and a photomultiplier tube with a Peltier-cooled PbS detector. Samples were measured in screw-top, gas-tight quartz cuvettes (path = 10 mm) and were prepared by diluting 40 µL of CuNC stock solutions in toluene (3 mL). Background spectra were recorded for clean toluene solvent.

Nuclear magnetic resonance (NMR) spectra were recorded on a Bruker Avance IIIHD 400 spectrometer fitted with a BBFOz probe, operating at 400.13 MHz for ^{1}H NMR spectra and 161.98 MHz for $^{31}P\{^1H\}$ NMR spectra. ^{1}H NMR chemical shifts were referenced internally to residual solvent resonances (d_6-benzene, δ_H = 7.16 ppm), and referenced externally against $SiMe_4$, where δ_H = 0 ppm. $^{31}P\{^1H\}$ spectra were referenced externally against H_3PO_4, where δ_P = 0 ppm. Samples were prepared by first evaporating hexane suspensions of CuNCs to dryness; the CuNCs were then suspended in a small volume of a d_6-benzene / d_6-acetone mixture and recollected by centrifugation. This was crucial in order to remove residual protio-solvent from the sample. The particles were then dried by evaporation and d_6-benzene (500 µL) was added to suspend the particles for analysis.

X-ray photoelectron spectra (XPS) were recorded using an Axis Supra (Kratos Analytical) instrument, using the monochromated Kα X-ray line of an Al anode. The pass energy was set to 20 eV with a step size of 0.1 eV. The samples were electrically insulated from the sample holder and charges were compensated. Spectra were referenced at 284.8 eV using the C–C bound of the C 1s orbital. As-synthesised CuNC samples were prepared by drop-casting nanocrystal films onto clean Si substrates. Post-CO_2RR CuNC samples were analysed directly on glassy carbon electrodes and were rinsed with deionised water to remove K_2CO_3 / $KHCO_3$ from the sample.

Electrochemical methods

Electrochemical impedance spectroscopy (EIS) was used to determine the electrochemical cell resistance (R_{cell}) and the charge-transfer resistance (R_{CT}); fitting details for the latter are given below. Four spectra were measured at the open-circuit potential, using 41 points between 1 MHz and 100 Hz, using a sinus amplitude of 20 mV and a pause time of 0.6 s between each frequency. The value for resistance compensation was taken either from the Nyquist plot (taking the value of Re(Z) at the minimum value of $-$Im(Z) before the charge-transfer arc), or from the plot of $|Z|$ against frequency, using the asymptotic value of $|Z|$. Where EIS was used to monitor ligand stripping intermittently during electrocatalysis, the chronoamperometry experiment was first stopped, then EIS was carried out under steady-state conditions. Chronoamperometry was then continued until the next time point was reached. Further details of these experiments are provided below.

Cyclic voltammetry (CV) and *square-wave voltammetry* (SWV) were carried out using a three-electrode set-up in a glass vial. The working electrode was a glassy-carbon disc, the counter electrode was a Pt wire, and the quasi-reference electrode was a Ag wire. The electrolyte was 0.1 M $[^nBu_4N][PF_6]$ in anhydrous acetonitrile, previously stored under N_2; all measurements were carried out under an atmosphere of N_2. Samples were prepared by drop-casting CuNCs from hexane suspensions onto the glassy-carbon disc. Voltammetric stripping of the ligands was investigated by CV, sweeping the potential in the cathodic direction from −0.25 V to −2.2 V vs Ag wire, at a scan rate of 50 mV s^{-1}. The same potential limits were used in SWV experiments, where: the equilibration time was 3 s; the step height was 2 mV; the pulse height was 20 mV; and the pulse width was 100 ms, giving a scan rate of 10 mV s^{-1}. In all cases, the NC film remained intact on the electrode. Similar CV conditions were used to study the free ligands in solution. In that case, a background scan was measured, and the ligand was then dissolved in the electrolyte. A 5 Hz filter was applied in all cases to reduce noise, and potentials were referenced by the addition of ferrocene at the end of each experiment (E, Fc^+/Fc = 0 V). To convert these potentials to the SHE scale, we made use of the following literature values:

- E, Fc^+/Fc = +0.4 V vs SCE in MeCN / [^{n}NBu$_4$][PF$_6$] [1]
- E, SCE = +0.24 V vs SHE [2]

While errors in the potential conversion could be introduced, one should bear in mind that they would be systematic and therefore the trend in Figure 5 would hold in any case.

The electrochemical CO_2 reduction reaction (CO_2RR) was assessed using a poly(methyl methacrylate) electrochemical cell. The working electrode was a planar glassy-carbon plate (2.5 × 2.5 cm^2, type 2, Alfa Aesar), the counter electrode was a Pt foil, and the reference electrode was Ag/AgCl (Innovative Instruments, leak-free series), positioned near the working electrode using an ethylene tetrafluoroethylene (ETFE) nut and Nano-Tight sleeve (from IDEX). Aqueous $KHCO_3$ (0.1 M) was used as the electrolyte (2000 μL in each half of the cell). The cathode and anode compartments were separated by a Selemion anion-exchange membrane (AGC Engineering). The exposed surface areas of the working and counter electrodes were approximately 1.5 cm^2. Copper foils acted as contact electrodes to connect the cell to the potentiostat (Biologic SP-300). CO_2 gas (Air Liquide) was sparged through 6 × 8 mm^2 frits (Adams & Chittenden) from the bottom of the cell in both anode and cathode compartments at a rate of 5 sccm (regulated with a Bronkhorst gas flow-controller). The gas was vented from the anode compartment to the atmosphere, whilst the gas from the cathode compartment directly entered an in-line gas chromatograph for analysis (SRI). For liquid product analysis, high-performance liquid chromatography (HPLC) was carried out using an UltiMate 3000 instrument (Thermo Scientific). Voltages were converted to the RHE scale by using a calibrated reference electrode as in **Equation S1**.

Equation S1

$$E_{\mathrm{RHE}} = E_{\mathrm{Ag/AgCl}} + 0.0591 \times \mathrm{pH} + E^{o}_{\mathrm{Ag/AgCl}}$$

Where $E^{o}_{\mathrm{Ag/AgCl}}$ = 0.206 V at 298 K and $E_{\mathrm{Ag/AgCl}}$ is the working potential.

Electrolyte preparation. Milli-Q water and high purity K_2CO_3 (99.995%) was used to prepare the aqueous electrolyte; trace metal impurities were then removed using Chelex resin (100 sodium form, 50-100 mesh, dry). The resin was first stirred over HCl (0.5 M) for 1 hour, decanted and washed with five equivalent volumes of water. It was then stirred over NaOH (0.5 M) at 50 ºC for 2 hours, decanted and washed with five equivalent volumes of water. Finally, K_2CO_3 (0.05 M) was stirred over the activated resin for 24 hours, and then decanted from the resin for use in electrochemistry. Prior to use in electrochemical experiments, K_2CO_3 was sparged for 30 minutes with CO_2 to generate $KHCO_3$ (0.1 M).

Gas product analysis by gas chromatography (GC). The GC was calibrated using five calibration gas mixtures containing H_2, CO, CH_4, C_2H_4 and C_2H_6 (Carbagas, SAPHIR, class 3). Calibration was done with an input gas-flow of 5 sccm and venting gas-flow of 5.5 sccm. The Faradaic efficiencies for gas products ($FE_{product}$ / %) were calculated according to **Equation S2**, where R is the gas constant (8.314 J K^{-1} mol^{-1}), T is the temperature (293.15 K), $n_{e,product}$ is the number of electrons required to form the gas product (2 for CO, 2 for H_2, 8 for methane, 12 for ethylene, 14 for ethane), $C_{product}$ is the concentration of gas produced / ppm, F is the Faraday constant (96,485 C mol^{-1}), I is the average current measured at the time of the GC measurement / A, and t_{fill} is the filling time of the GC (12 seconds). When $I > 1$ mA in the experiment, the background current and C_{CO}, C_{H2} values (*i.e.* amounts of products in ppm) from the blank glassy carbon electrode were subtracted in the calculation of FE.

Equation S2

$$\mathrm{FE}_{\mathrm{product}} = \frac{101.325 \times 10^{-9} \times R \times T \times n_{\mathrm{e,\ product}} \times C_{\mathrm{product}}}{F \times I \times t_{\mathrm{fill}}} \times 100$$

Surface area measurements. Electrochemically active surface areas (ECSA / cm^2) were determined using capacitance methods. Cyclic voltammograms (CVs) were first recorded between −0.350 and −0.300 V vs Ag/AgCl (in a region where no redox activity takes place) at incremented scan-rates between 4 and 32 mV s^{-1}. The geometric current-density values for the charging (J_c) and discharging (J_d) capacitance were taken at −0.325 V vs Ag/AgCl. The difference between these values ($J_{total} = J_d - J_c$ / μA cm^{-2}) was plotted against the scan rate, ν / V s^{-1}. The slope of this linear plot yields the capacitance value for the sample, C_{sample} / μF cm^{-2}. This process was repeated for a clean glassy carbon electrode in order to obtain a reference capacitance value for a flat surface ($C_{GC} = 27.8$ μF cm^{-2}). Division of C_{sample} by C_{GC} then gives a surface roughness factor (S.R.F.), as in **Equation S3**. With the S.R.F. value in hand, the geometric surface area of the electrode (S_{geom}, 1.5 cm^2) can be modified to give current density values normalised by the electrochemically active surface area, J_{ECSA} / μA cm^{-2}, as in **Equation S4**. Finally, to compare intrinsic activities of the catalysts, the overall CO_2RR selectivity was also considered (**Equation S5**).

Equation S3

$$\mathrm{S.R.F.} = \frac{C_{\mathrm{sample}}}{C_{\mathrm{GC}}}$$

Equation S4

$$J_{\mathrm{ECSA}} = \frac{I}{\mathrm{S.R.F.} \times S_{\mathrm{geom}}}$$

Equation S5

$$J_{\mathrm{CO2RR}} = J_{\mathrm{ECSA}} \times \frac{\%\mathrm{FE}_{\mathrm{CO2RR}}}{100}$$

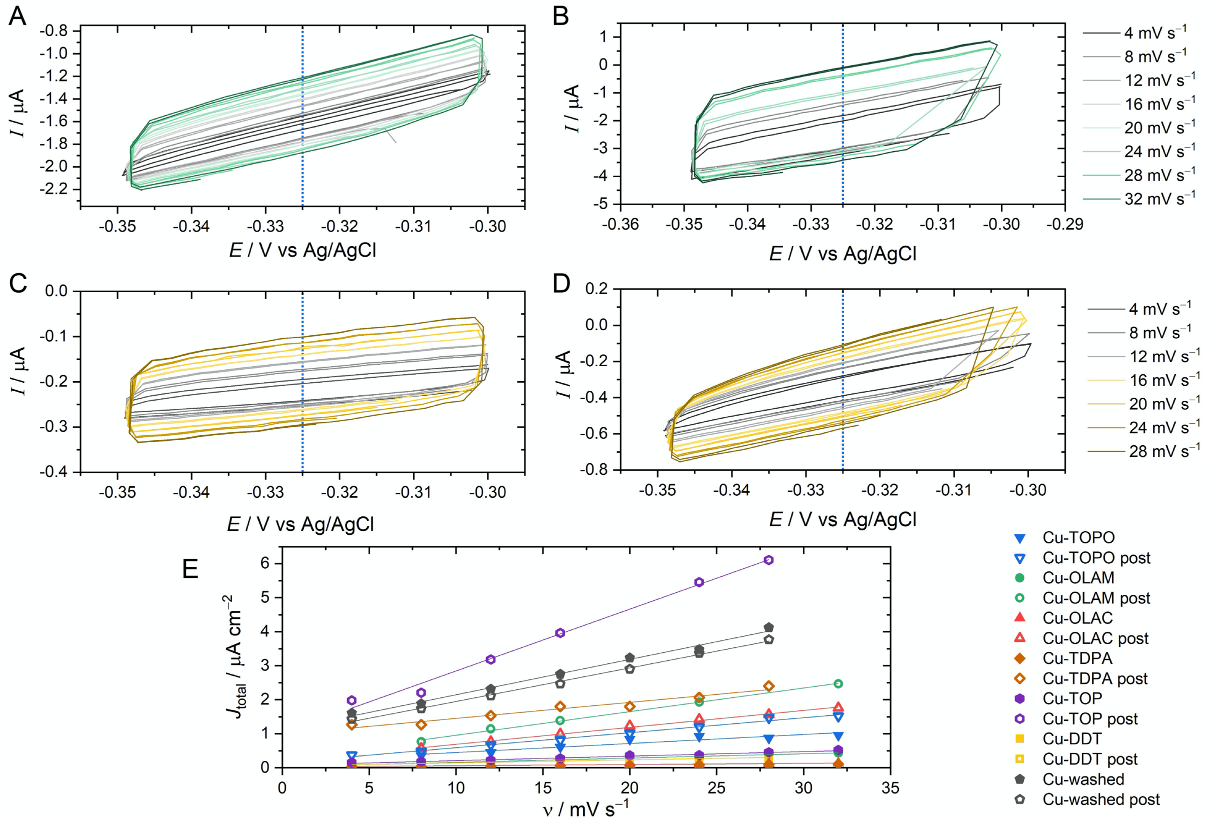

Figure S1. Representative examples of cyclic voltammograms used to determine the capacitance and the electrochemically active surface areas for NC samples. A) **Cu-OLAM**, as-synthesised. B) **Cu-OLAM**, post-CO_2RR. C) **Cu-DDT**, as-synthesised. D) **Cu-DDT**, post-CO_2RR. The blue dotted lines at –0.325 V vs Ag/AgCl indicate where J_c and J_d values were taken to calculate J_{total}. E) J_{total} plotted against the scan-rate to determine the sample capacitance, showing representative examples for every sample.

Synthesis of 5 nm, spherical CuNCs[3]

In a three-neck round-bottomed flask, tri-*n*-octylamine (10 mL) was degassed under dynamic vacuum at 130ºC for 30 minutes. The flask was then refilled with N_2 gas and cooled to 50ºC. Tetradecylphosphonic acid (139 mg, 0.5 mmol) and copper(I) acetate (123 mg, 1 mmol) were added to the flask, forming a green, cloudy mixture. The mixture was heated to 180ºC, where the mixture turned light brown. After 30 minutes, the mixture was rapidly heated to 270ºC, quickly forming a red, opaque mixture. After 30 minutes at 270ºC, the mixture was cooled to room temperature and was transferred to centrifugation vials. To each 2.5 mL portion of the crude reaction mixture, hexane (5 mL) and ethanol (15 mL) were added. The particles were isolated by centrifugation at 5000 rpm for 15 minutes, and the supernatant was discarded. The particles were then washed using hexane (5 mL) and ethanol (15 mL), and again isolated after centrifugation. Finally, the particles were recovered and combined into a single suspension using toluene (6 mL total) and were stored under N_2 in a freezer (−30ºC).

Yield (based on ICP-OES): 62.7 mg Cu (0.987 mmol, 98.7%)

Diameter (based on TEM, counting 100 particles): 5.24 ± 0.71 nm

Ligand exchange procedure

A 2000 µL aliquot of the CuNC stock suspension was transferred to a centrifugation vial (*ca.* 10 mg Cu based on ICP-OES). A second solution of $[Me_3O][BF_4]$ (Meerwein's salt, *ca.* 20 mg) in MeCN (1 mL) was added and the mixture was stirred for 1 minute, then left to stand for 10 minutes. The mixture was centrifuged at 5000 rpm for 10 minutes, and the supernatant was discarded. DMF (750 μL) was added to the particles, forming a red suspension that was then diluted with toluene (750 μL). The new ligand was then added neat, using *ca.* 100 μL of liquid compounds (OLAM, OLAC, DDT or TOP) and *ca.* 50 mg of solid compounds (TOPO or TDPA); on addition of the new ligands, the red DMF suspensions darkened. The mixture was vigorously shaken for 1 minute, sonicated for 30 seconds, and then left to stand for 2 hours. After this time, acetone (2 mL) was added as an anti-solvent and the mixture was centrifuged at 5000 rpm for 15 minutes; the supernatant was discarded. The particles were then washed by resuspending in hexane (1 mL) and precipitating with acetone (5 mL); the supernatant was again discarded after centrifugation. Finally, the particles were recovered in hexane (2 mL) and stored under N_2 at −30°C.

Following ICP-OES analysis, these stock solutions were diluted to a common concentration of 1.1 μg μL^{-1}. Electrochemical measurements could then be carried out at identical mass-loadings using identical volumes to prepare the catalyst films.

The CuNC control sample with no surface ligands was prepared from the as-synthesized **Cu-TOPO**. The latter was drop-cast on a glassy carbon electrode and then submerged in acetone for 2 hours. The electrode was dipped three times in fresh acetone and then air-dried. Weakly bound acetone ligands were removed from the surface using a single linear potential sweep inside the electrochemical cell. A prominent acetone desorption wave was observed around −0.15 V vs RHE. After this treatment, the washed CuNC film displayed high ECSA and low R_{CT} values as reported in the discussion.

Table S1. Retention of 5 nm, spherical CuNCs during the ligand exchange process, determined by ICP-OES.

	Mass, Cu before exchange / mg	Mass, Cu after exchange / mg	NC retention / %
Cu-OLAM	9.94	6.24	63
Cu-OLAC	9.94	6.13	62
Cu-DDT	9.94	7.80	78
Cu-TOP	9.94	4.11	41
Cu-TOPO	9.94	5.46	55
Cu-TDPA	9.94	6.12	62

Characterising data for CuNC catalysts (TEM, UV-vis, XPS, FT-IR, NMR)

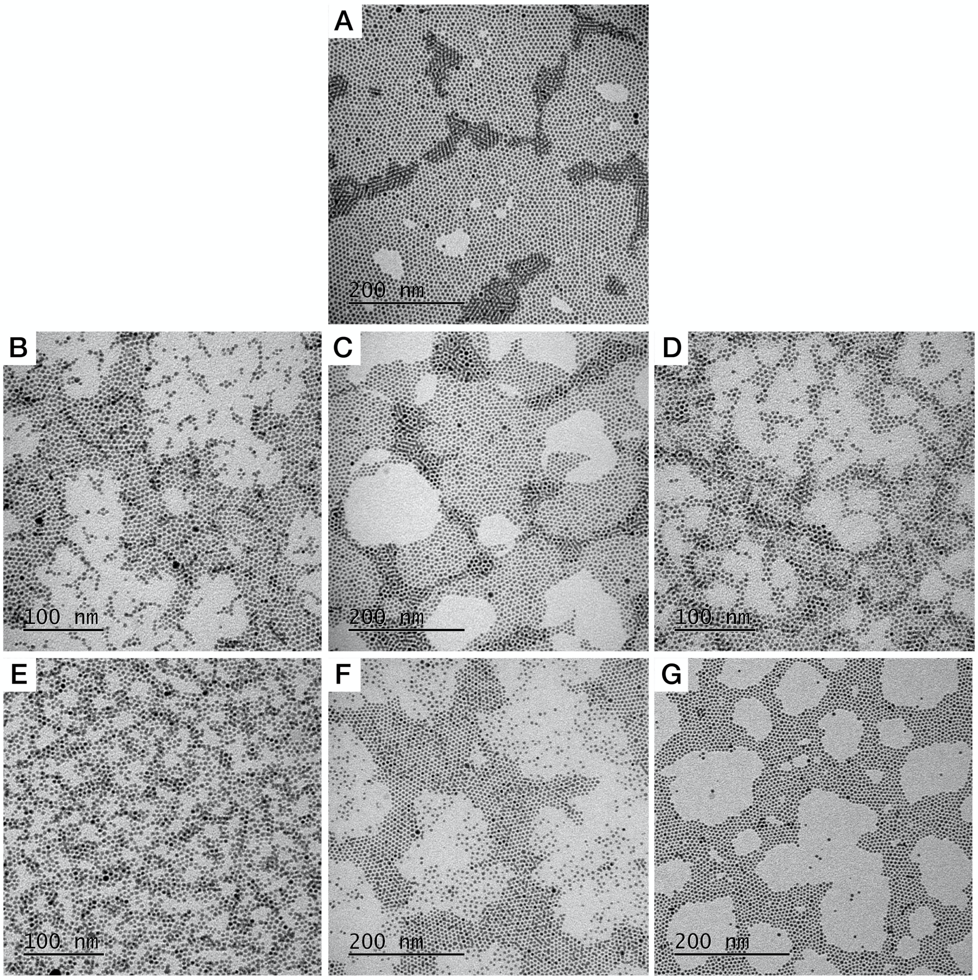

Figure S2. TEM images of the as-synthesised spherical CuNCs (A, $d = 5.24 \pm 0.71$ nm) and those following functionalisation with new ligands, where the NCs are stabilised by: B) OLAM, $d = 5.16 \pm 0.74$ nm; C) OLAC, $d = 5.51 \pm 0.60$ nm; D) DDT, $d = 4.87 \pm 0.50$ nm; E) TOP, $d = 5.10 \pm 0.48$ nm; F) TOPO, $d = 5.26 \pm 0.55$ nm; and (G) TDPA, $d = 5.25 \pm 0.58$ nm. Note that the small size variation derives from the fact that the NCs comes from different batches, not from etching during ligand exchange.

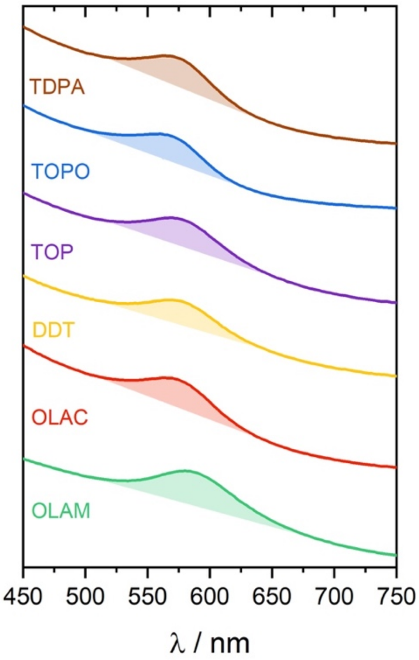

Figure S3. UV-vis absorption spectra of CuNCs following ligand exchange. The peaks are shaded for clarity. Peak positions were all approximately at 575 nm. All samples were measured as toluene solutions at room temperature, with equivalent concentrations of Cu.

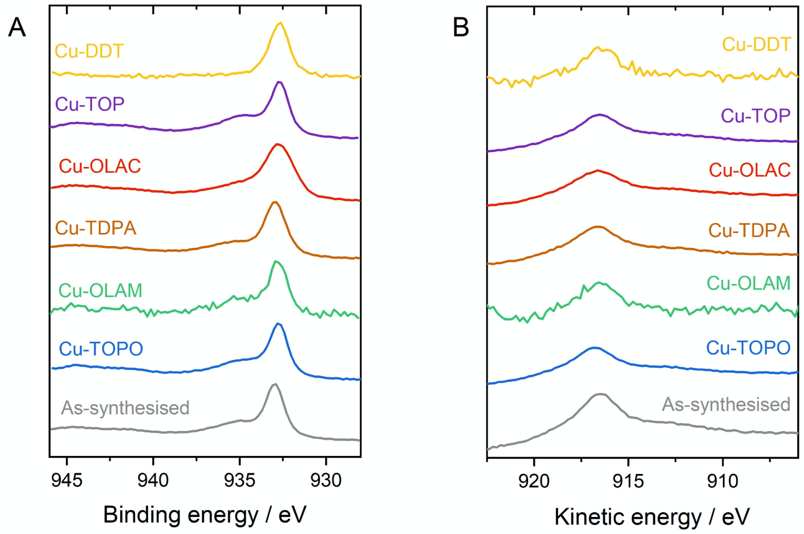

Figure S4. X-ray photoelectron spectra of (A) the Cu2$p_{3/2}$ region and (B) the Cu LMM Auger region, showing that the surface state of the CuNCs remains unchanged following ligand exchange.

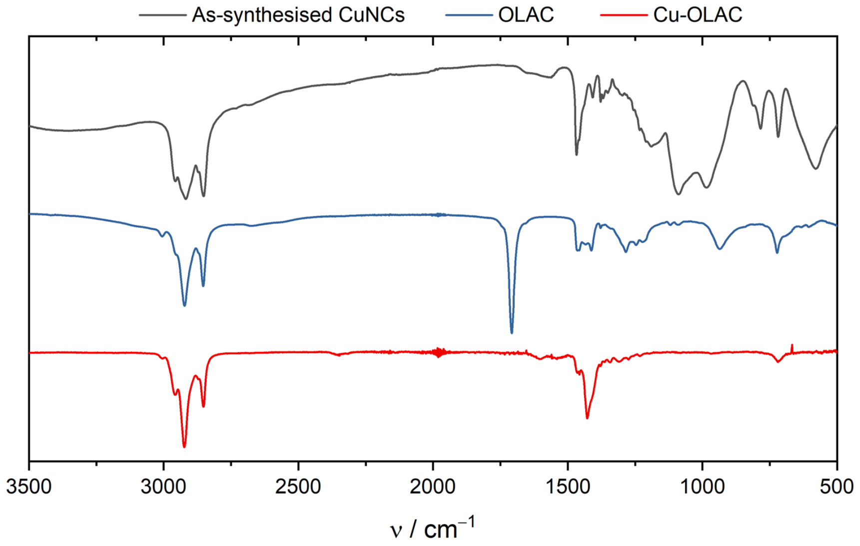

Figure S5. FT-IR spectrum of **Cu-OLAC** NCs following ligand exchange. The IR spectra of the free ligand and the as-synthesised CuNCs are also shown for comparison.

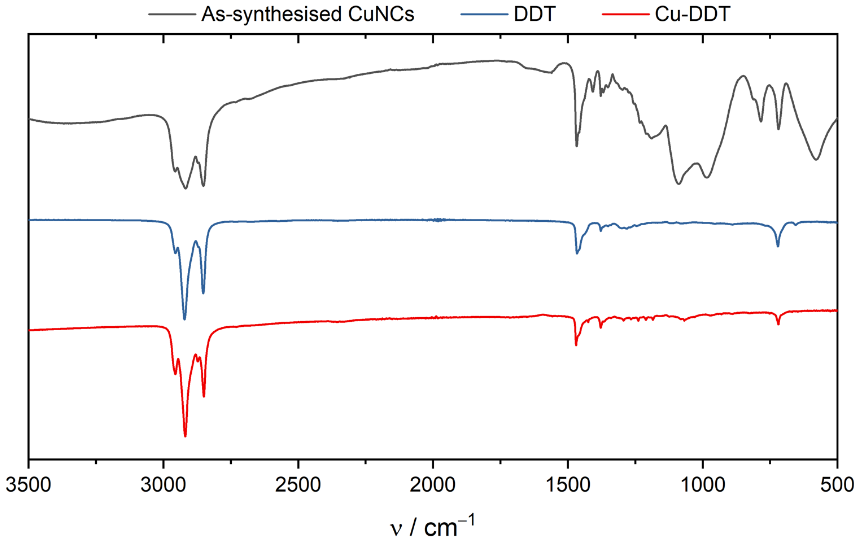

Figure S6. FT-IR spectrum of **Cu-DDT** NCs following ligand exchange. The IR spectra of the free ligand and the as-synthesised CuNCs are also shown for comparison.

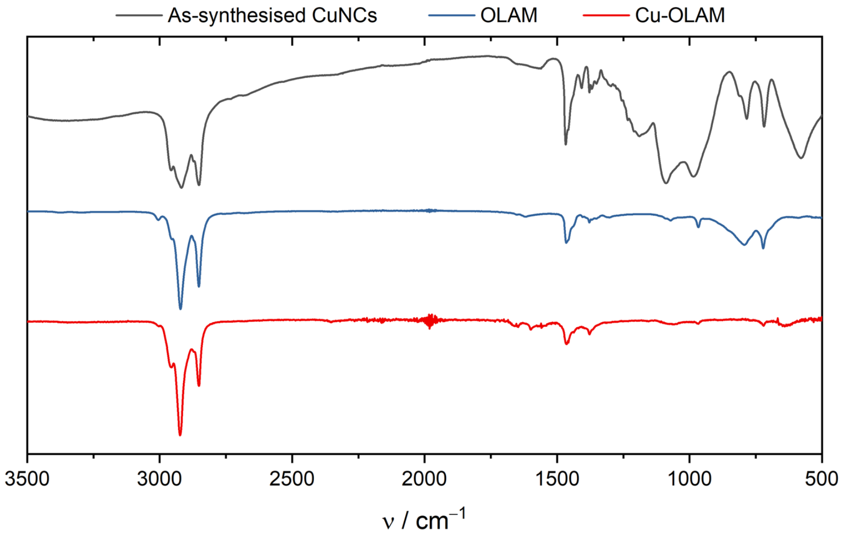

Figure S7. FT-IR spectrum of **Cu-OLAM** NCs following ligand exchange. The IR spectra of the free ligand and the as-synthesised CuNCs are also shown for comparison.

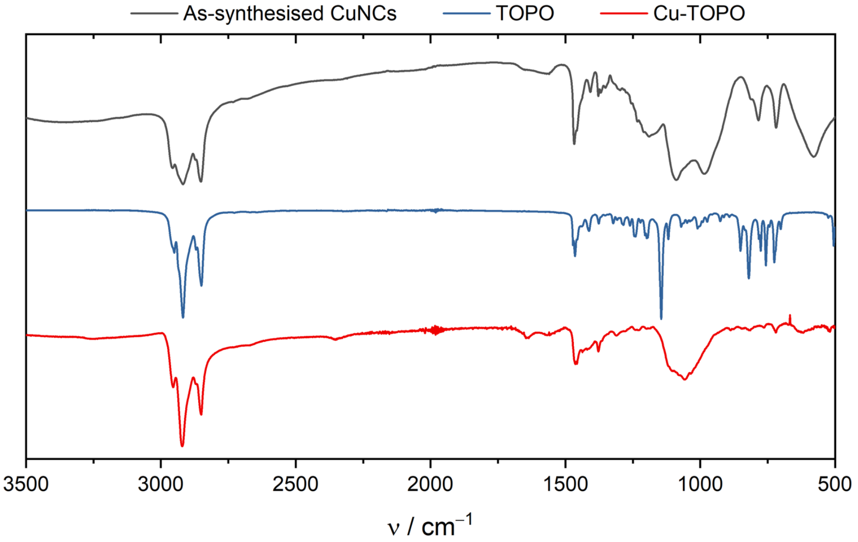

Figure S8. FT-IR spectrum of **Cu-TOPO** NCs following ligand exchange. The IR spectra of the free ligand and the as-synthesised CuNCs are also shown for comparison.

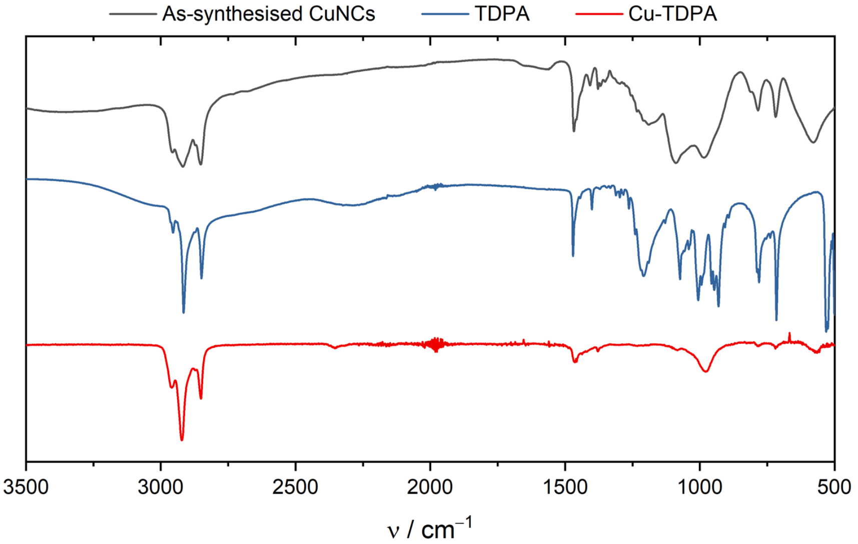

Figure S9. FT-IR spectrum of **Cu-TDPA** NCs following ligand exchange. The IR spectra of the free ligand and the as-synthesised CuNCs are also shown for comparison.

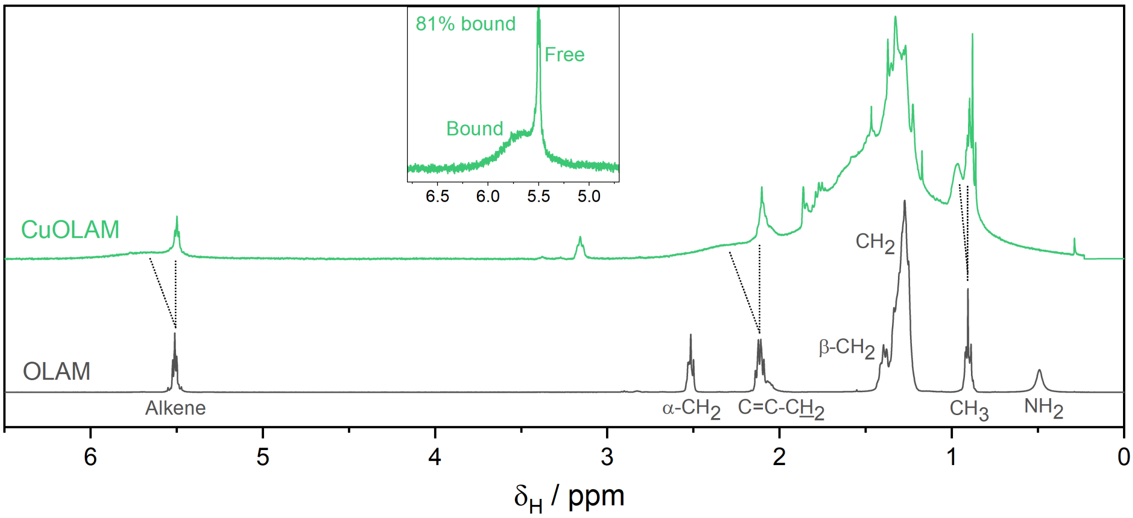

Figure S10. ^{1}H NMR spectra of free OLAM and **Cu-OLAM** NCs, both measured in d_6-benzene. Peaks are labelled with assignments to individual proton environments, and dotted lines indicate how these resonances change in **Cu-OLAM**. A focussed view of the alkene region is shown inset; fitting and integration of these two peaks indicates that 81% of the OLAM in the sample is found in a bound state.

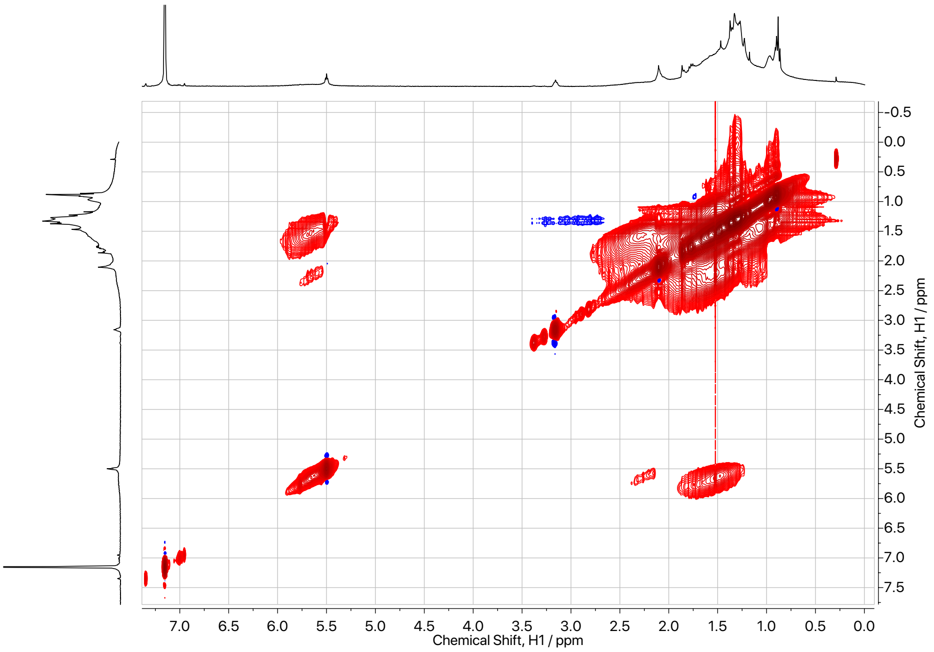

Figure S11. ^{1}H-^{1}H NOESY spectrum of **Cu-OLAM**, measured in d_6-benzene. Intense, negative NOE cross-peaks are observed between the alkene and methylene resonances, consistent with OLAM bound on the CuNC surface.[4] Here, negative cross-peaks mean that they share the same sign as the diagonal peaks (indicated by the red colour).

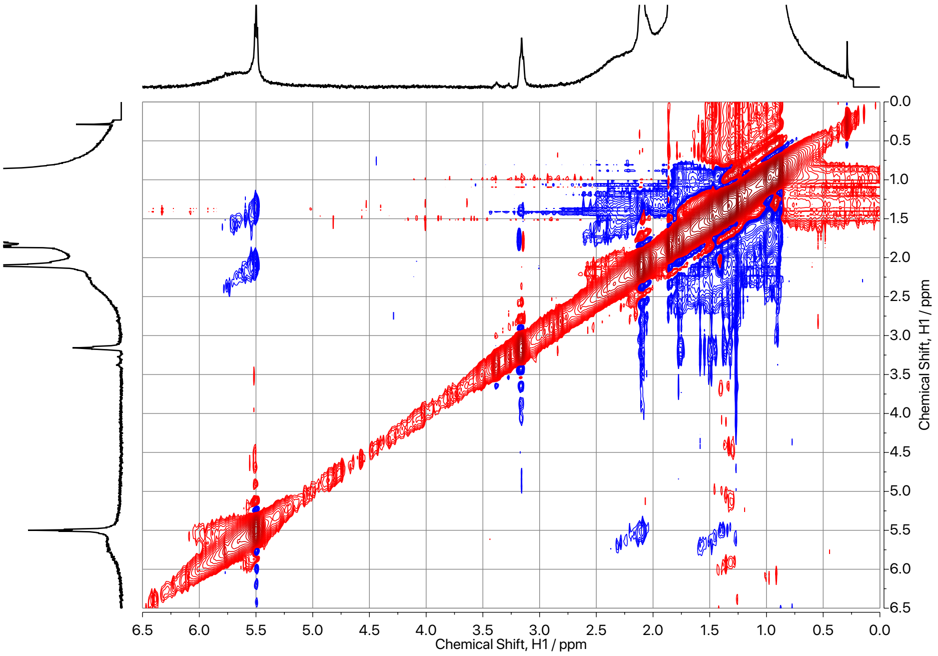

Figure S12. ^{1}H-^{1}H ROESY spectrum of **Cu-OLAM**, measured in d_6-benzene. Positive cross-peaks (blue) confirm that these arise due to NOE interactions rather than chemical exchange between bound and free states of OLAM.[4]

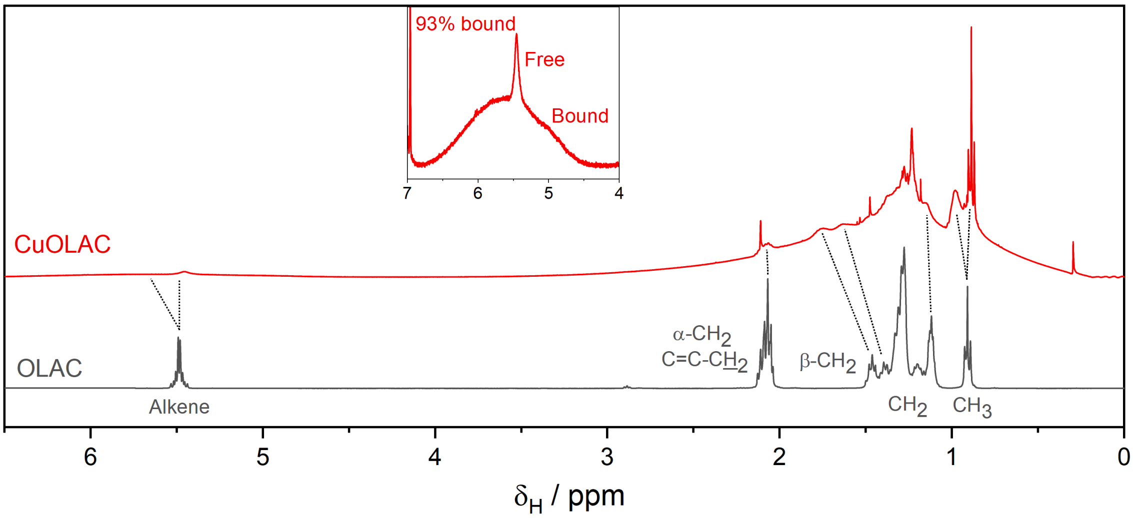

Figure S13. ^{1}H NMR spectra of free OLAC and **Cu-OLAC** NCs, both measured in d_6-benzene. Peaks are labelled with assignments to individual proton environments, and dotted lines indicate how these resonances change in **Cu-OLAC**. A focussed view of the alkene region is shown inset; fitting and integration of these two peaks indicates that 93% of the OLAC in the sample is found in a bound state.

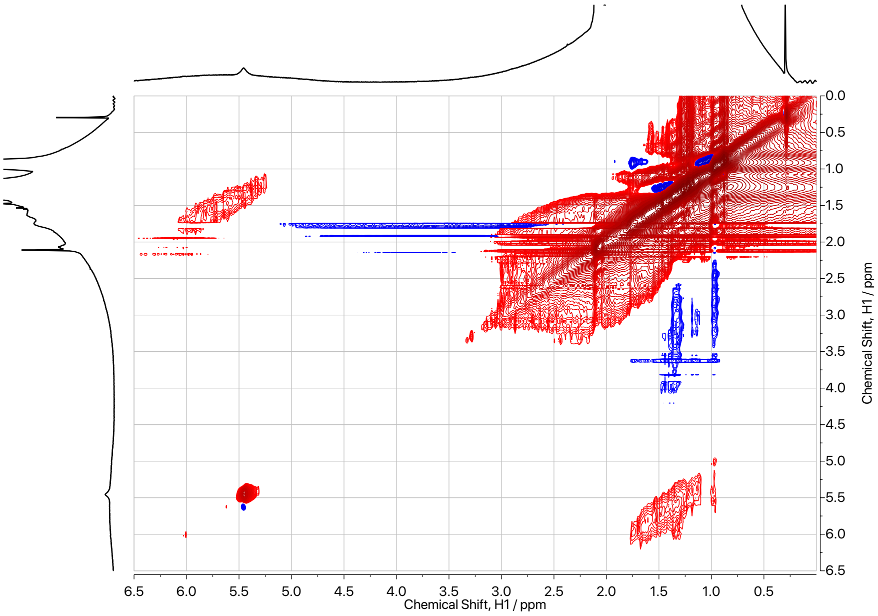

Figure S14. ^1H-^1H NOESY spectrum of **Cu-OLAC**, measured in d_6-benzene. Intense, negative NOE cross-peaks are observed between the alkene and methylene resonances, consistent with OLAC bound on the CuNC surface.[4]

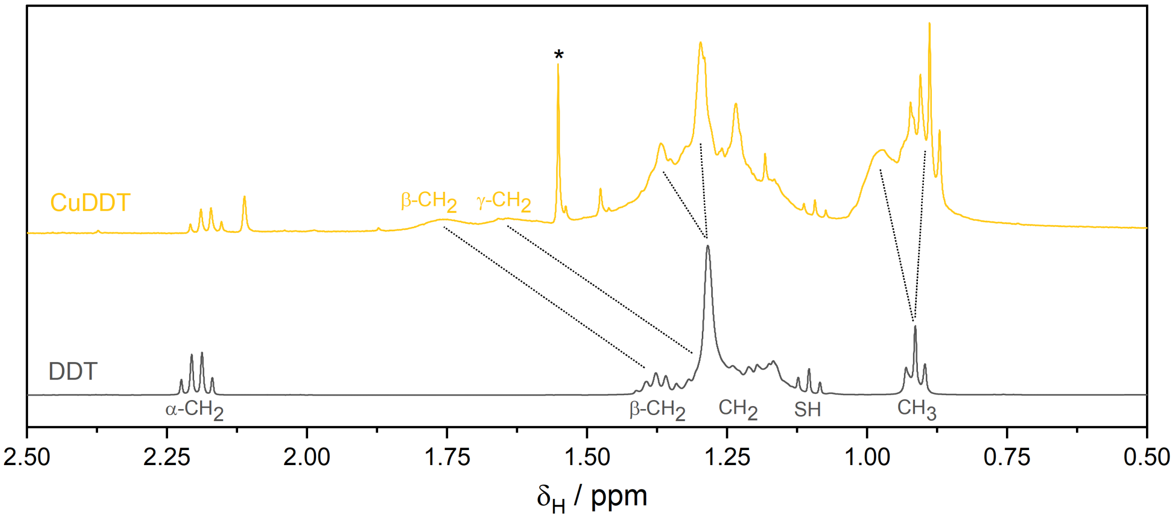

Figure S15. ^1H NMR spectra of free DDT and **Cu-DDT** NCs, both measured in d_6-benzene. Peaks are labelled with assignments to individual proton environments, and dotted lines indicate how these resonances change in **Cu-DDT**. Physisorbed DDT is present in the sample (confirmed by XPS), but approximately 75% is in a chemisorbed, thiolate state based on fitting and integration. A residual acetone resonance is marked by *.

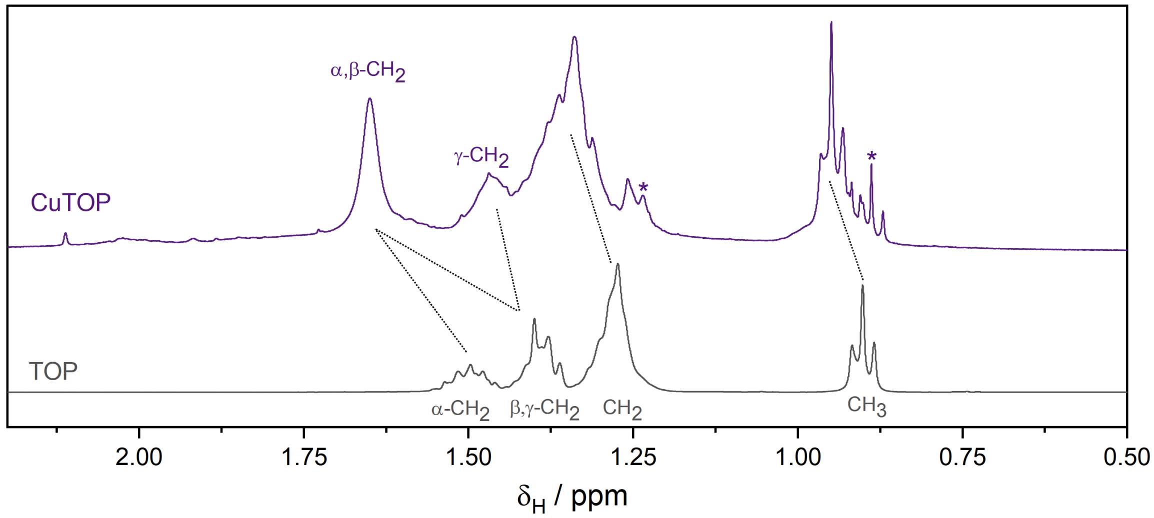

Figure S16. ^{1}H NMR spectra of free TOP and **Cu-TOP** NCs, both measured in d_6-benzene. Peaks are labelled with assignments to individual proton environments, and dotted lines indicate how these resonances change in **Cu-TOP**. No free TOP is observed in the NC sample. Residual hexane resonances are marked by *.

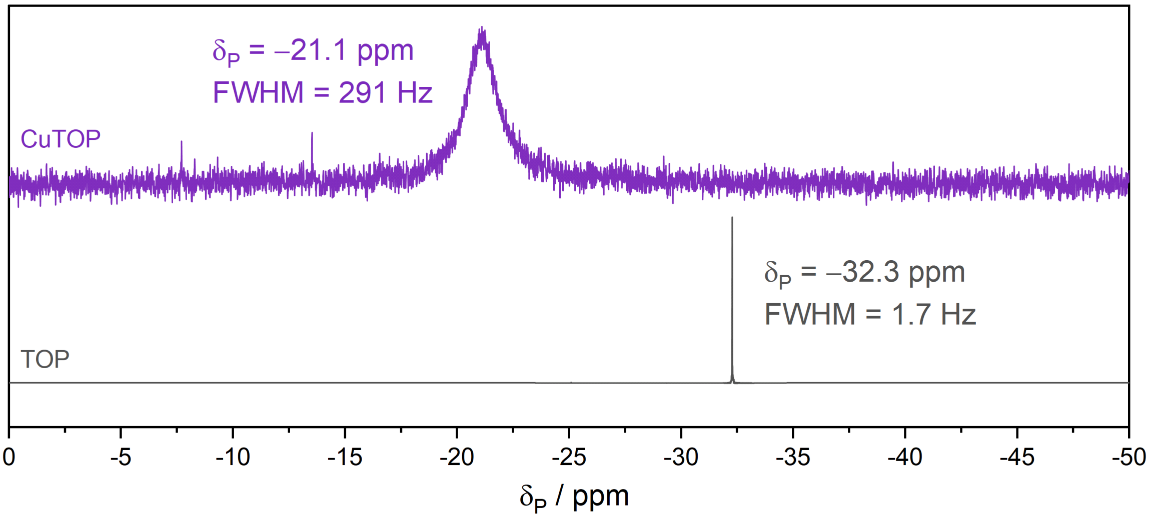

Figure S17. ^{31}P{^{1}H} NMR spectra of free TOP and **Cu-TOP** NCs, both measured in d_6-benzene. The large, positive change in chemical shift and the severe broadening of the phosphine resonance indicates that TOP is bound to the NC surface. No free TOP is observed in the NC sample. FWHM = full-width half-maximum.

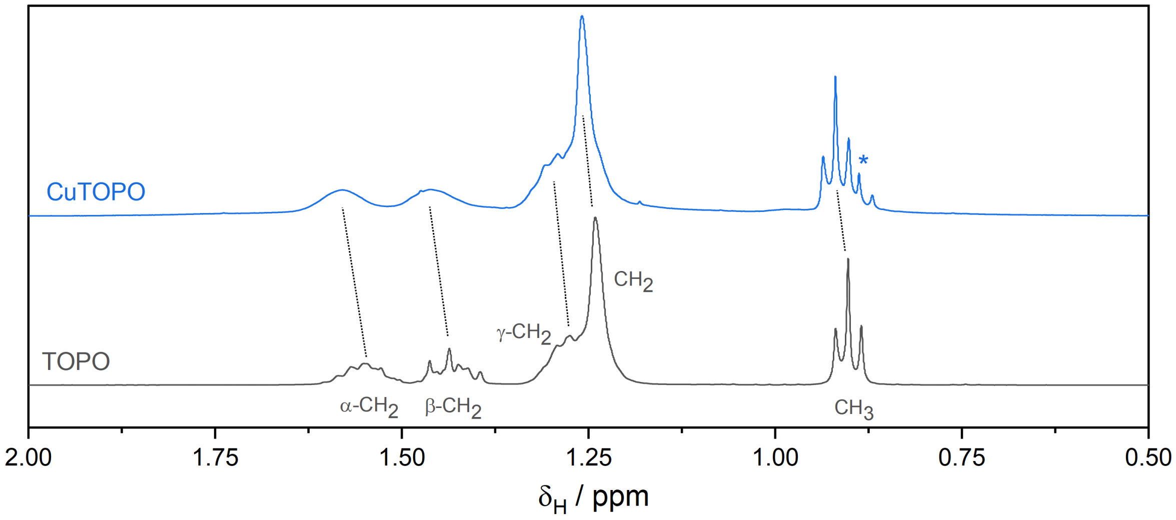

Figure S18. ^{1}H NMR spectra of free TOPO and **Cu-TOPO** NCs, both measured in d_6-benzene. Peaks are labelled with assignments to individual proton environments, and dotted lines indicate how these resonances change in **Cu-TOPO**. No free TOPO is observed in the NC sample. A residual hexane resonance is marked by *.

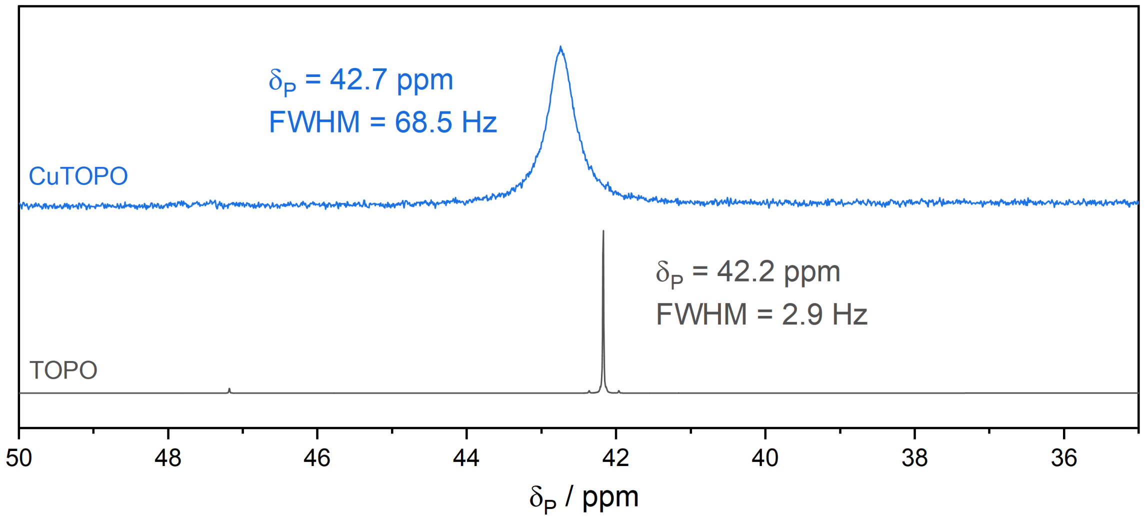

Figure S19. $^{31}P\{^1H\}$ NMR spectra of free TOPO and **Cu-TOPO** NCs, both measured in d_6-benzene. The large, positive change in chemical shift and the severe broadening of the phosphine oxide resonance indicates that TOPO is bound to the NC surface. No free TOPO is observed in the NC sample. FWHM = full-width half-maximum.

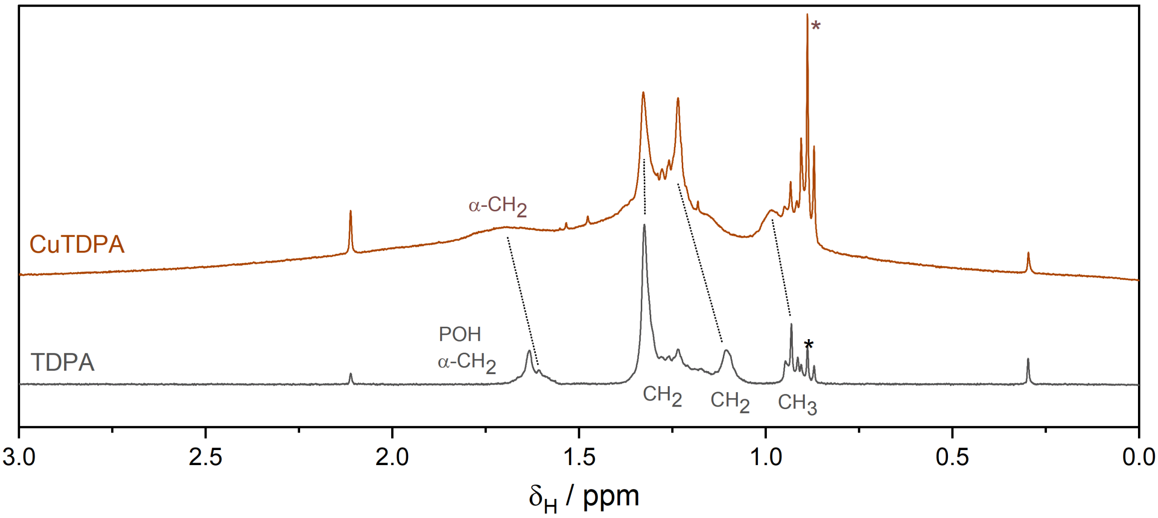

Figure S20. ^1H NMR spectra of free TDPA and **Cu-TDPA** NCs, both measured in d_6-benzene. Peaks are labelled with assignments to individual proton environments, and dotted lines indicate how these resonances change in **Cu-TDPA**. No free TDPA is observed in the NC sample. A residual hexane resonance is marked by *.

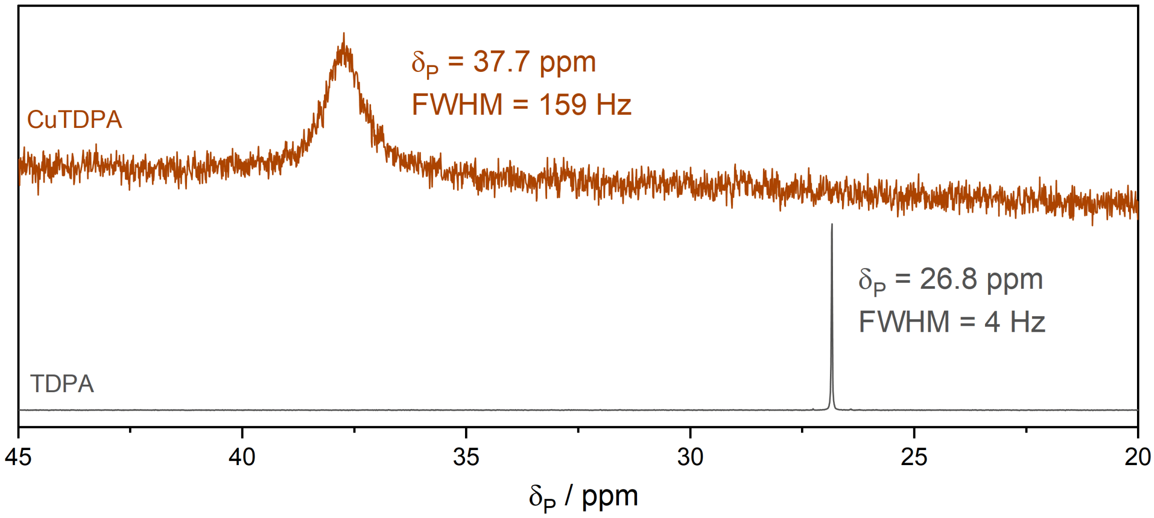

Figure S21. $^{31}P\{^1H\}$ NMR spectra of free TDPA and **Cu-TDPA** NCs, measured in d_6-DMSO and d_6-benzene, respectively. The large, positive change in chemical shift and the severe broadening of the phosphonic acid resonance indicates that TDPA is bound to the NC surface. No free TDPA is observed in the NC sample. FWHM = full-width half-maximum.

Additional electrochemistry data

Table S2. Summary of Faradaic efficiencies for all products in the CO_2RR with the CuNC catalysts studied in this work. “Other” products include trace amounts of acetate, ethylene glycol, ethanol and propanol. Gas products were quantified by gas chromatography and liquid products by high-performance liquid chromatography.

Catalyst	%FE, CO	%FE, CH_4	%FE, C_2H_4	%FE, Formate	%FE, Other	%FE, H_2	Sum, %FE
Washed	2.78	1.25	3.86	25.11	1.54	67.30	101.8
Cu-TOPO	5.34	4.57	7.43	29.43	0.97	55.34	103.1
Cu-OLAM	3.05	2.06	5.05	19.03	2.01	71.76	103.0
Cu-TDPA	5.01	2.84	7.98	29.39	2.29	55.20	102.7
Cu-OLAC	4.31	0.36	11.58	26.7	2.51	53.08	98.54
Cu-TOP	2.41	1.74	2.39	32.63	2.81	60.88	102.9
Cu-DDT	5.08	0.39	0.16	13.33	1.16	81.55	101.7

For the modelling of electrochemical impedance spectra (EIS), we recognised that our cell is a complex system. For example, the resistance between the electrode and the nanocrystals, and that between the nanocrystals and the electrolyte, could be described by two different equivalent circuit components in a full model. There are also non-trivial contributions due to the mass transport in the electrolyte; these cannot be modelled by adding a simple Warburg diffusion term to the circuit because of the sparging CO_2 gas in the cell. Ultimately, we assumed that all of these additional factors would be similar for all of the CuNC catalysts, and we then simplified our model using a Randles cell, (**Figure S22**) so that we could extract the charge-transfer resistance values.

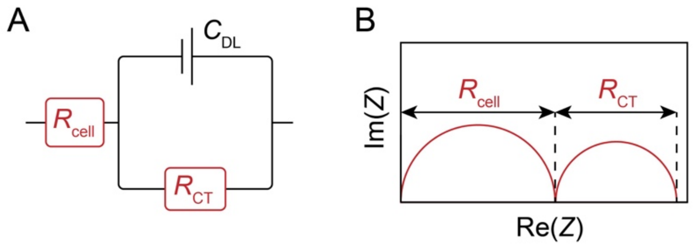

Figure S22. Details of the fitting of the EI spectra. A) Equivalent circuit diagram for the fit (Randles cell), where C_{DL} is a double-layer capacitance term. B) Cartoon of an idealised Nyquist plot, showing how R_{cell} and R_{CT} produce individual semi-circular arcs.

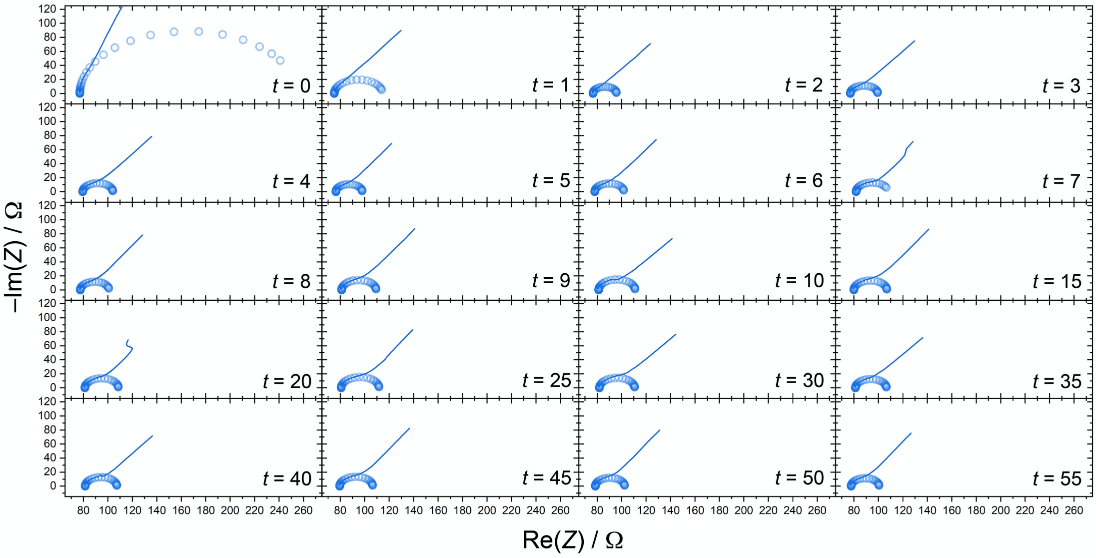

Figure S23. Impedance spectra measured intermittently between periods of CO_2RR electrolysis for **Cu-TOPO**, $E = -1.1$ V vs RHE. Time spent under CO_2RR conditions is indicated for each spectrum, given in minutes.

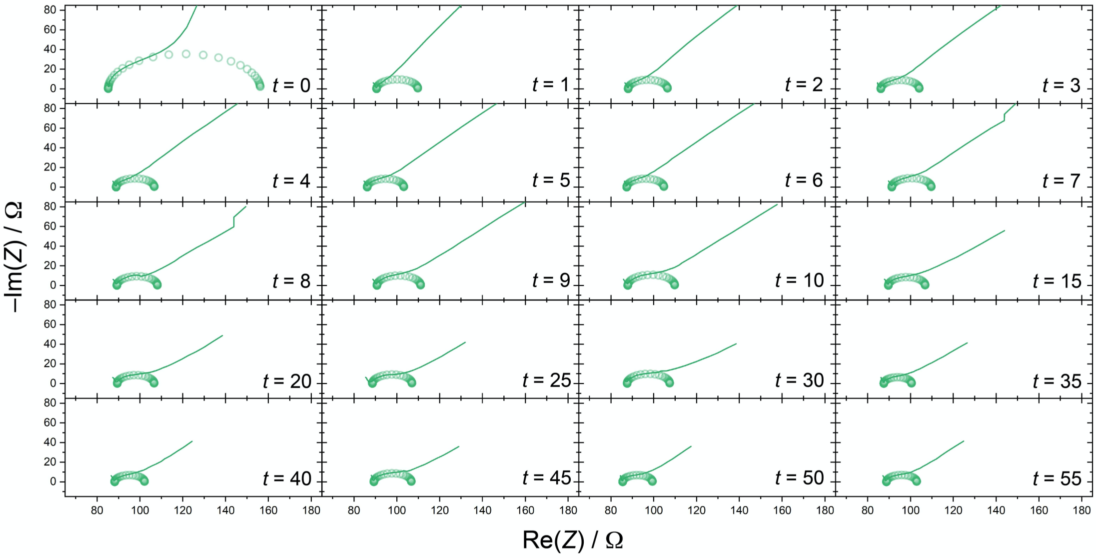

Figure S24. Impedance spectra measured intermittently between periods of CO_2RR electrolysis for **Cu-OLAM**, $E = -1.1$ V vs RHE. Time spent under CO_2RR conditions is indicated for each spectrum, given in minutes.

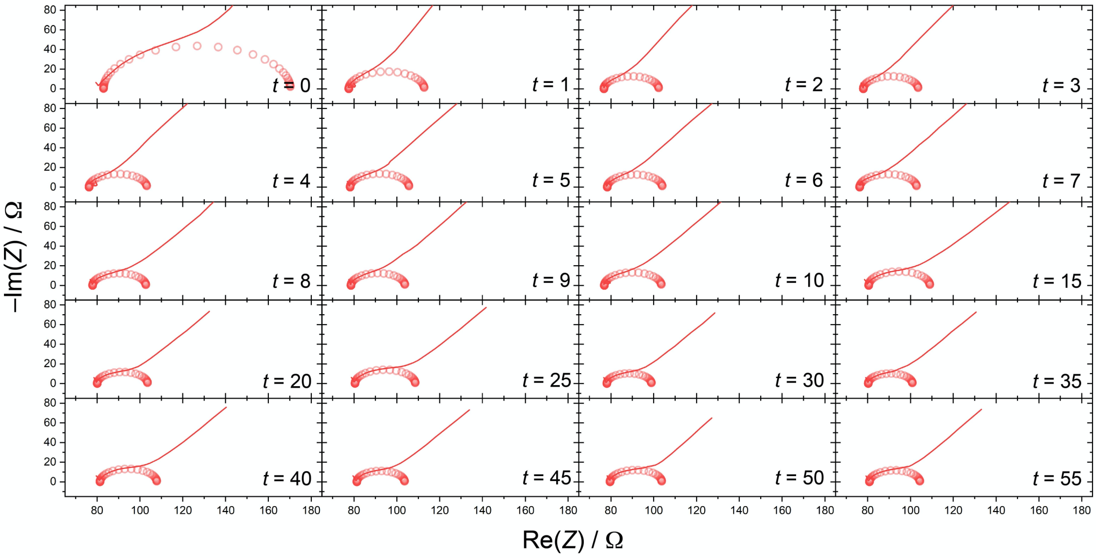

Figure S25. Impedance spectra measured intermittently between periods of CO_2RR electrolysis for **Cu-OLAC**, $E = -1.1$ V vs RHE. Time spent under CO_2RR conditions is indicated for each spectrum, given in minutes.

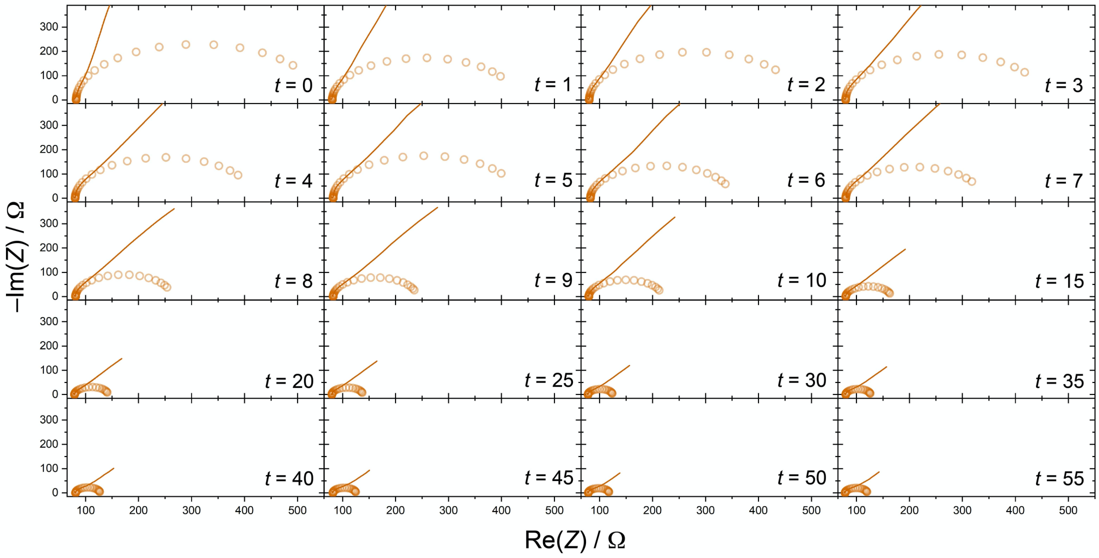

Figure S26. Impedance spectra measured intermittently between periods of CO_2RR electrolysis for **Cu-TDPA**, $E = -1.1$ V vs RHE. Time spent under CO_2RR conditions is indicated for each spectrum, given in minutes.

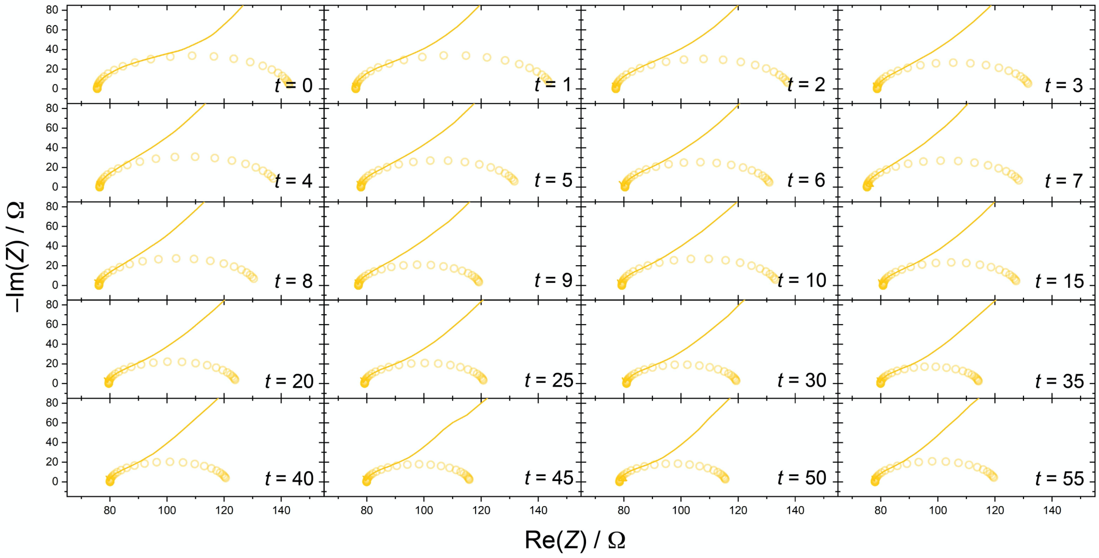

Figure S27. Impedance spectra measured intermittently between periods of CO_2RR electrolysis for **Cu-DDT**, $E = -1.1$ V vs RHE. Time spent under CO_2RR conditions is indicated for each spectrum, given in minutes.

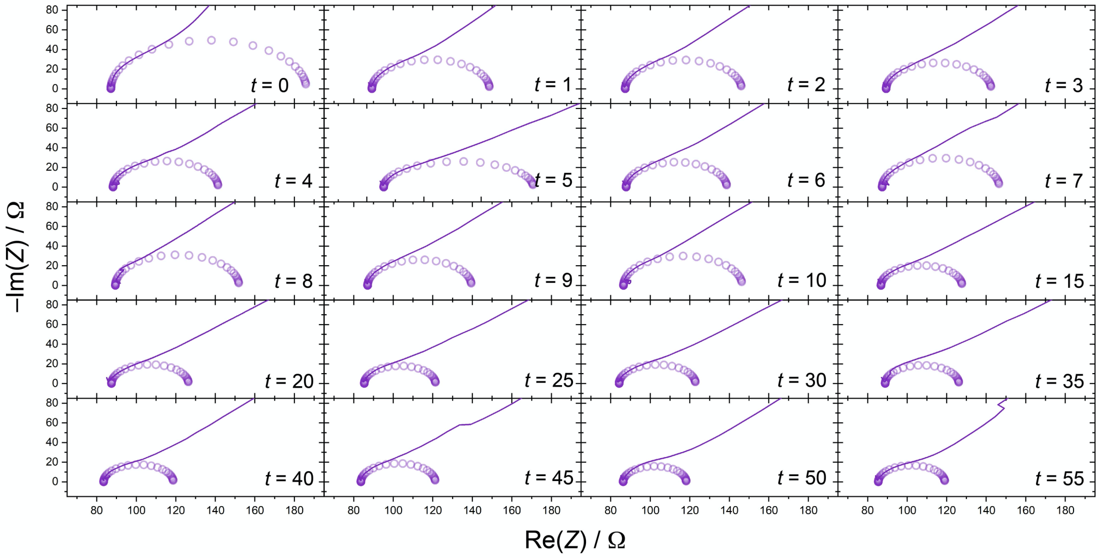

Figure S28. Impedance spectra measured intermittently between periods of CO_2RR electrolysis for **Cu-TOP**, $E = -1.1$ V vs RHE. Time spent under CO_2RR conditions is indicated for each spectrum, given in minutes.

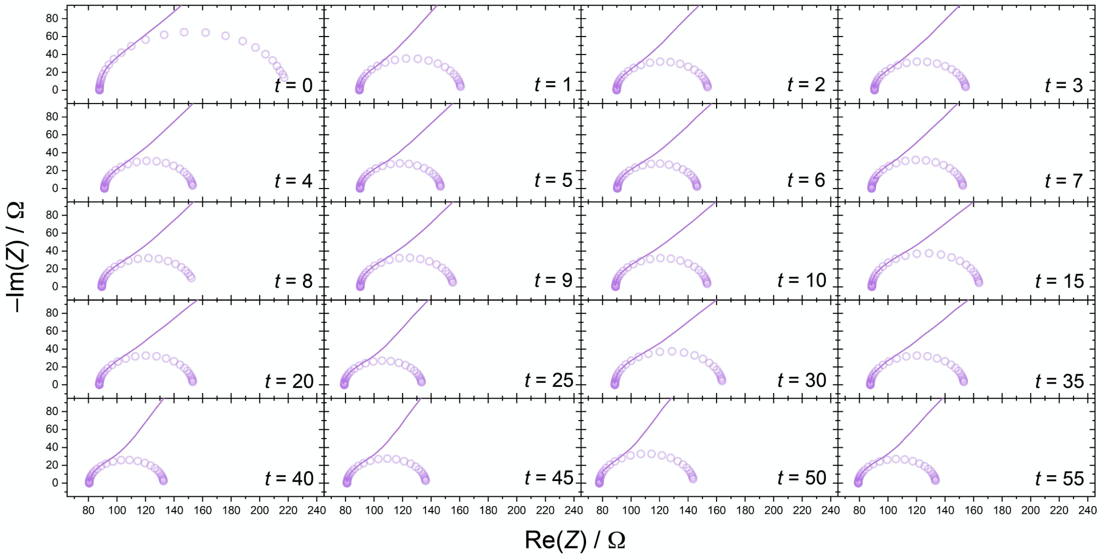

Figure S29. Impedance spectra measured intermittently between periods of CO_2RR electrolysis for **Cu-TOP**, $E = -0.9$ V vs RHE. Time spent under CO_2RR conditions is indicated for each spectrum, given in minutes.

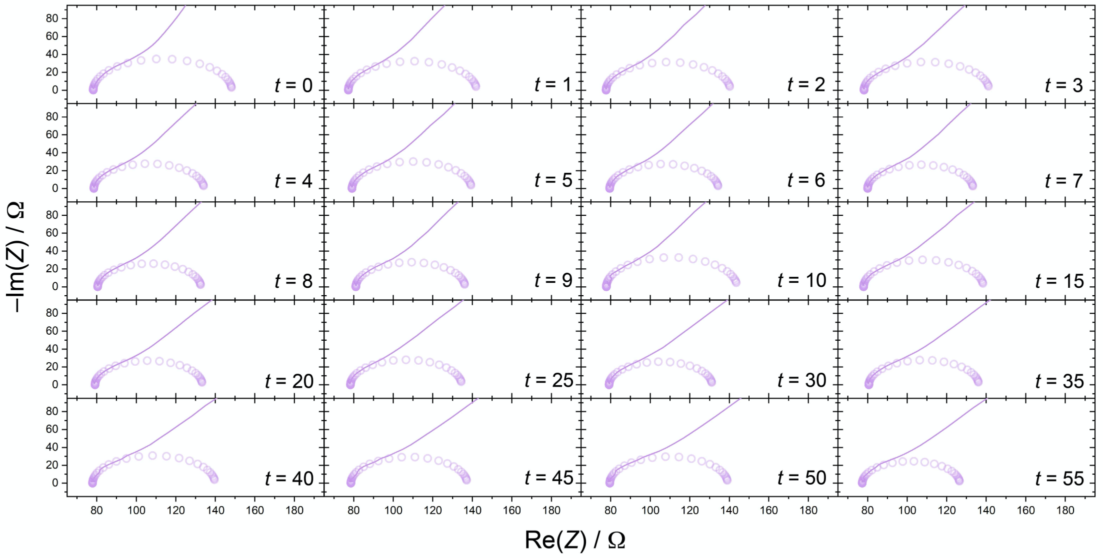

Figure S30. Impedance spectra measured intermittently between periods of CO_2RR electrolysis for **Cu-TOP**, $E = -0.7$ V vs RHE. Time spent under CO_2RR conditions is indicated for each spectrum, given in minutes.

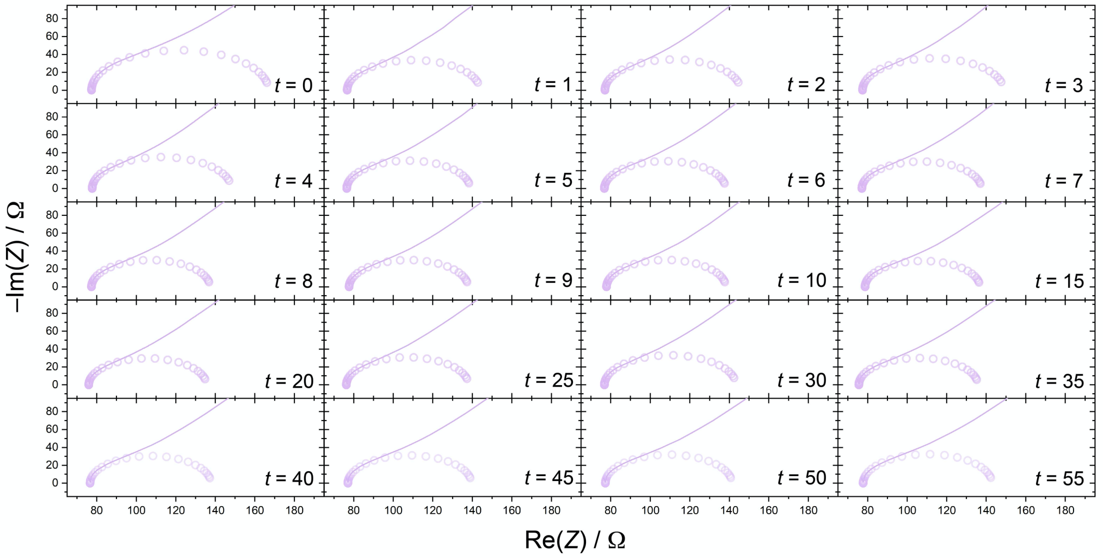

Figure S31. Impedance spectra measured intermittently between periods of CO_2RR electrolysis for **Cu-TOP**, $E = -0.5$ V vs RHE. Time spent under CO_2RR conditions is indicated for each spectrum, given in minutes.

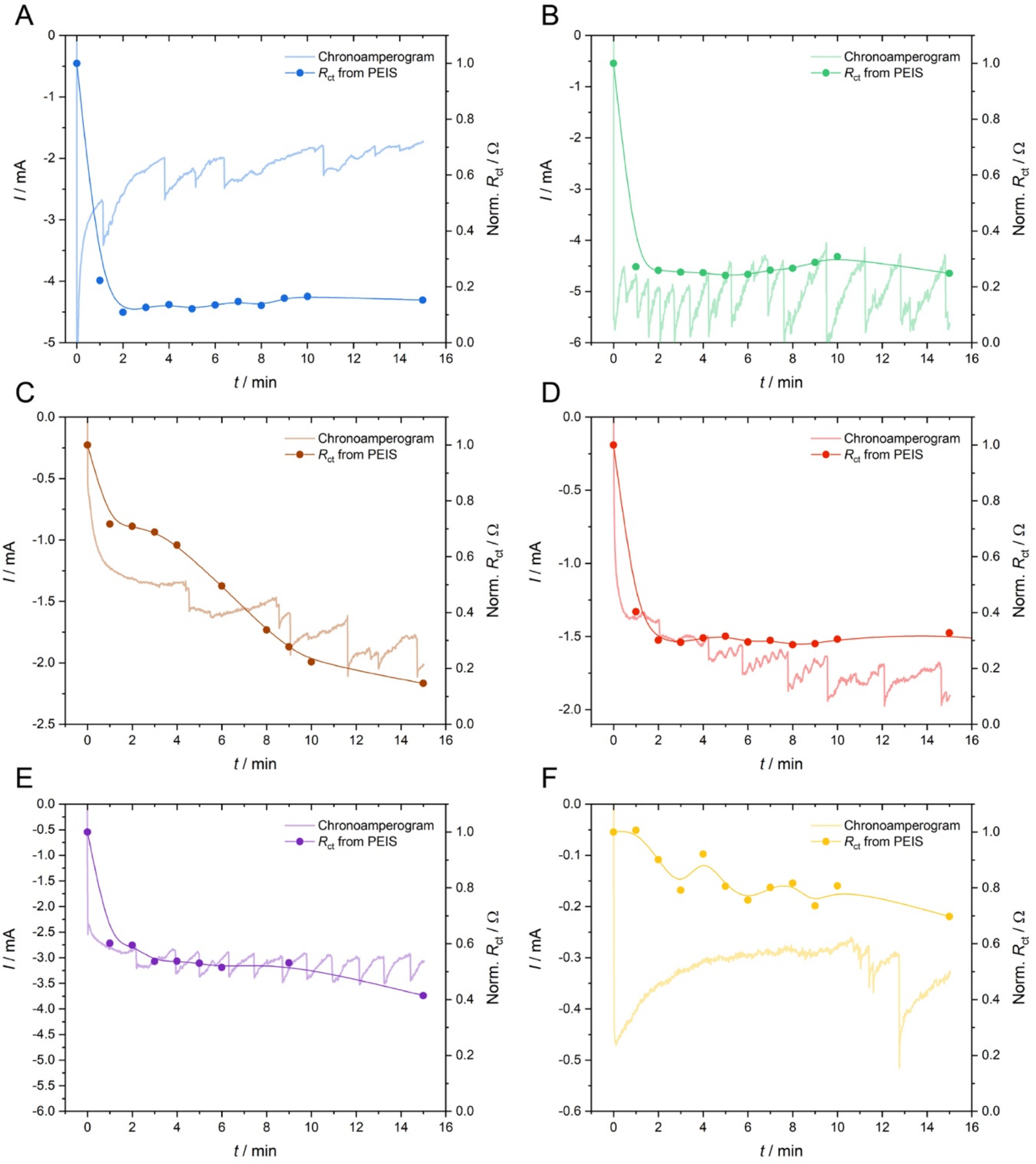

Figure S32. Comparisons of the charge-transfer resistance (R_{CT}) with the CO$_2$RR current (I), and their relationship in the beginning of the CO$_2$RR. All measured during CO$_2$RR electrolysis at –1.1 V vs RHE. A) **Cu-TOPO**; B) **Cu-OLAM**; C) **Cu-TDPA**; D) **Cu-OLAC**; E) **Cu-TOP**; and (F) **Cu-DDT**. For weakly bound ligands, R_{CT} drops very quickly and stabilises, at which point bubbling on the electrode is evident from the sharp spikes in current. For strongly bound ligands, R_{CT} decreases and stabilises more slowly, delaying the onset of bubbling. The spikes in the amperograms also correlate with the onset of gas products being detected by the GC, confirming that these features signal the onset of the CO$_2$RR. In comparison, the washed CuNC sample immediately attains a stable current value, and the CO$_2$RR begins immediately after the potential is applied (data not shown).

Additional XPS data

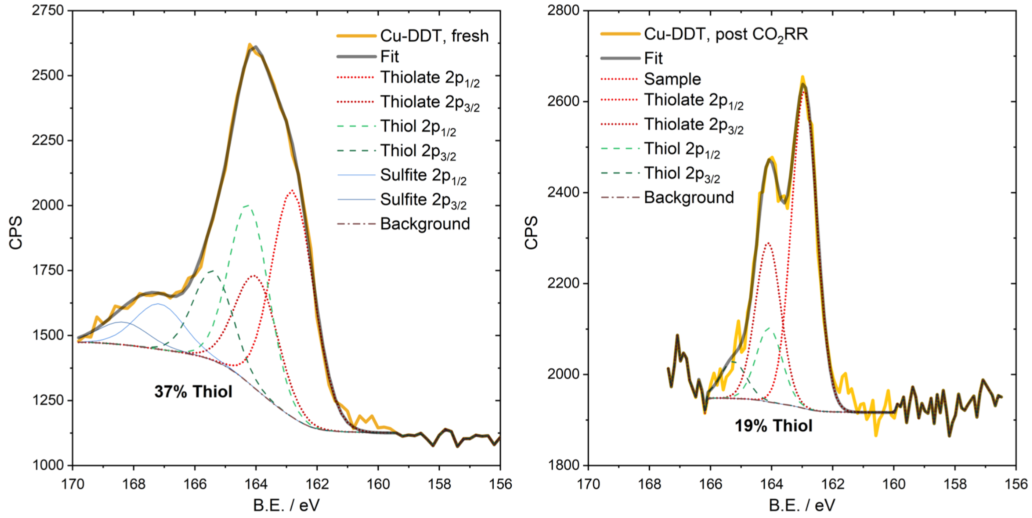

Figure S33. Fitting of the DDT S2p lines before (left) and after (right) CO_2RR electrolysis. For the as-synthesised sample, good fits were obtained for a three-component system. The thiol and thiolate components are discussed in the main text. The third, trace component is arbitrarily assigned as 'sulfite' and is likely an oxidised sulfur impurity. Following CO_2RR, the sulfite impurity is completely gone, as is much of the thiol. The %thiol contribution in each spectrum is indicated.

Morphological changes in the CO_2RR and EDX studies

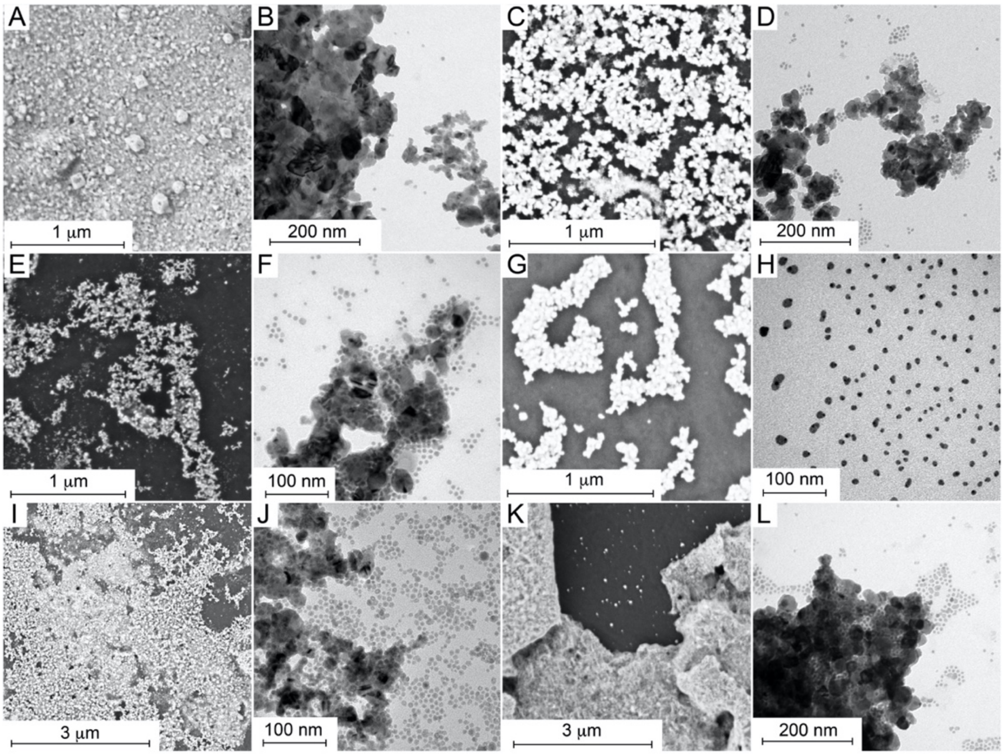

Figure S34. Study of the morphology of the 5 nm, spherical CuNCs following 1-hour CO_2RR electrolysis at –1.1 V vs RHE. SEM images were taken directly on the glassy carbon electrode. TEM images were taken after transferring the CuNCs to TEM grids by gently scratching of the electrode. A, B) SEM and TEM images of **Cu-TOPO**. C, D) SEM and TEM images of **Cu-OLAM**. E, F) SEM and TEM images of **Cu-TDPA**. G, H) SEM and TEM images of **Cu-OLAC**. I, J) SEM and TEM images of **Cu-TOP**. K, L) SEM and TEM images of **Cu-DDT**.

Figure S24 shows that all of the CuNC catalysts have some tendency to sinter into larger particles after applying the negative potential, in line with previous studies on Cu and other nanocrystal catalysts with small sizes.[5,6] While we expected **Cu-TOP** and **Cu-DDT** to be more resilient to sintering because of the ligands remaining bound to the surface, we could not observe any significant difference in the morphological changes observed depending on the ligands present on the surface.

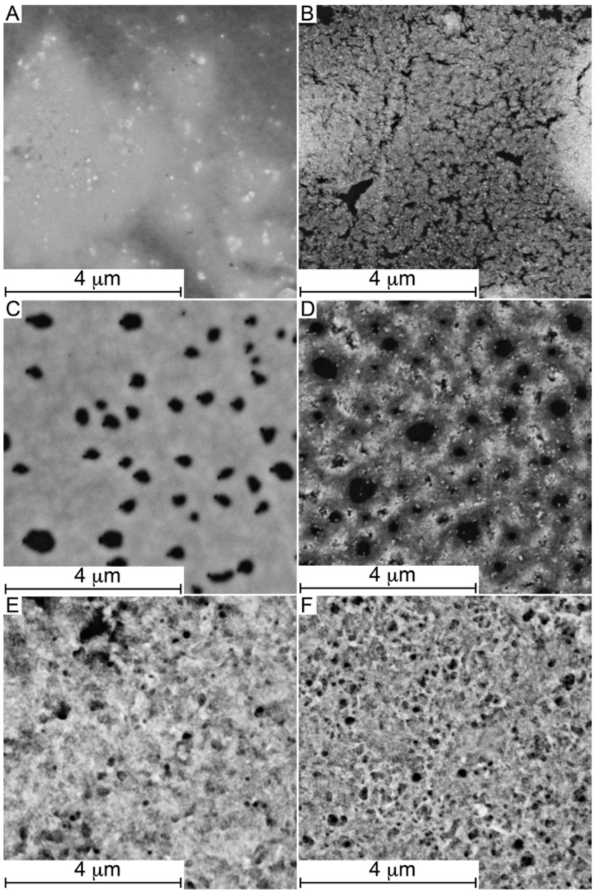

Figure S35. SEM images of as-synthesised CuNC catalyst films on the glassy carbon electrode, and those after CO_2RR electrolysis at –1.1 V vs RHE. A, B) **Cu-TOPO** before and after CO_2RR. C, D) **Cu-TOP** before and after CO_2RR. E, F) **Cu-DDT** before and after CO_2RR.

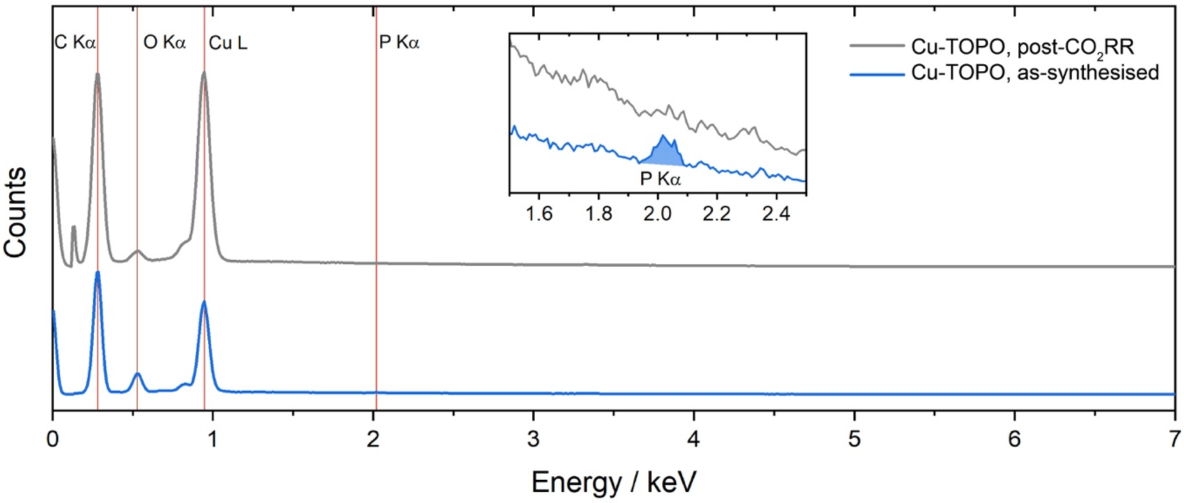

Figure S36. EDX spectra of **Cu-TOPO** before and after CO_2RR electrolysis at −1.1 V vs RHE. The inset spectra show a focussed view of the P Kα region, where the peaks are shaded for clarity. The spectra correspond to the images in Figure S25A,B.

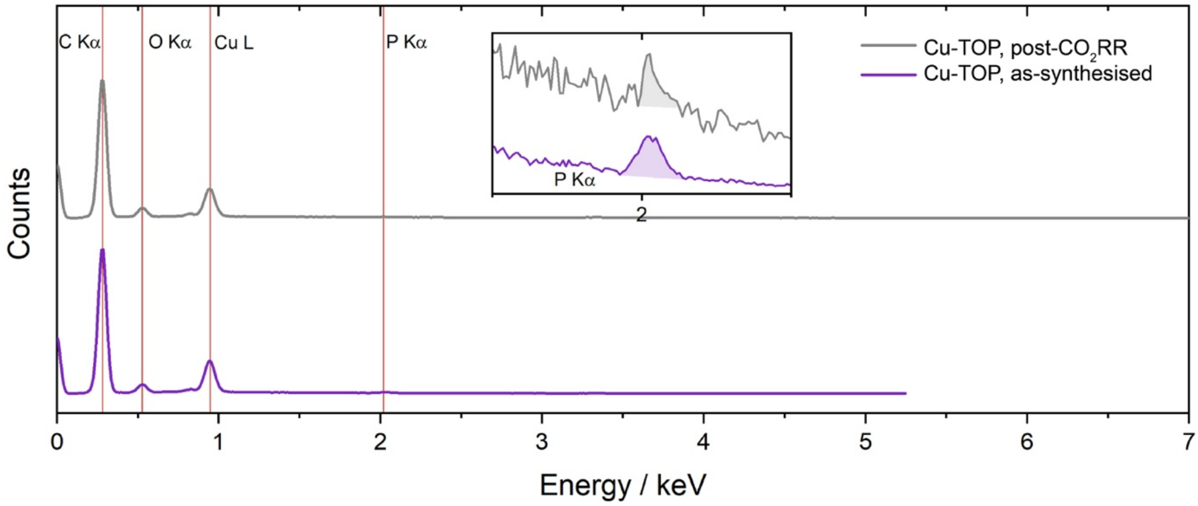

Figure S37. EDX spectra of **Cu-TOP** before and after CO_2RR electrolysis at −1.1 V vs RHE. The inset spectra show a focussed view of the P Kα region, where the peaks are shaded for clarity. The spectra correspond to the images in Figure S25C,D.

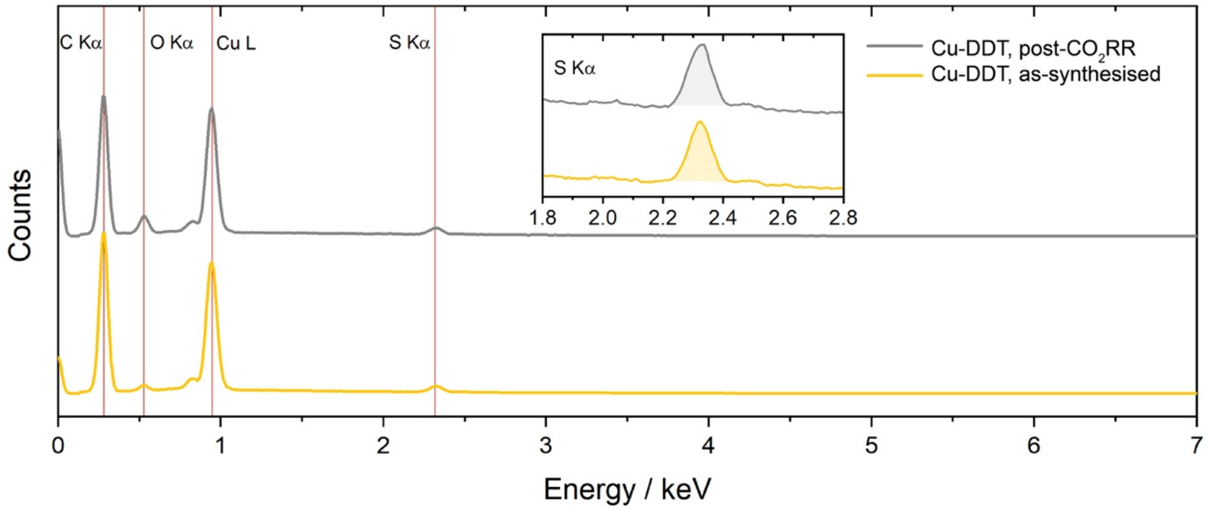

Figure S38. EDX spectra of **Cu-DDT** before and after CO_2RR electrolysis at −1.1 V vs RHE. The inset spectra show a focussed view of the S Kα region, where the peaks are shaded for clarity. The spectra correspond to the images in Figure S25E,F.

Cyclic voltammograms of free ligands in solution

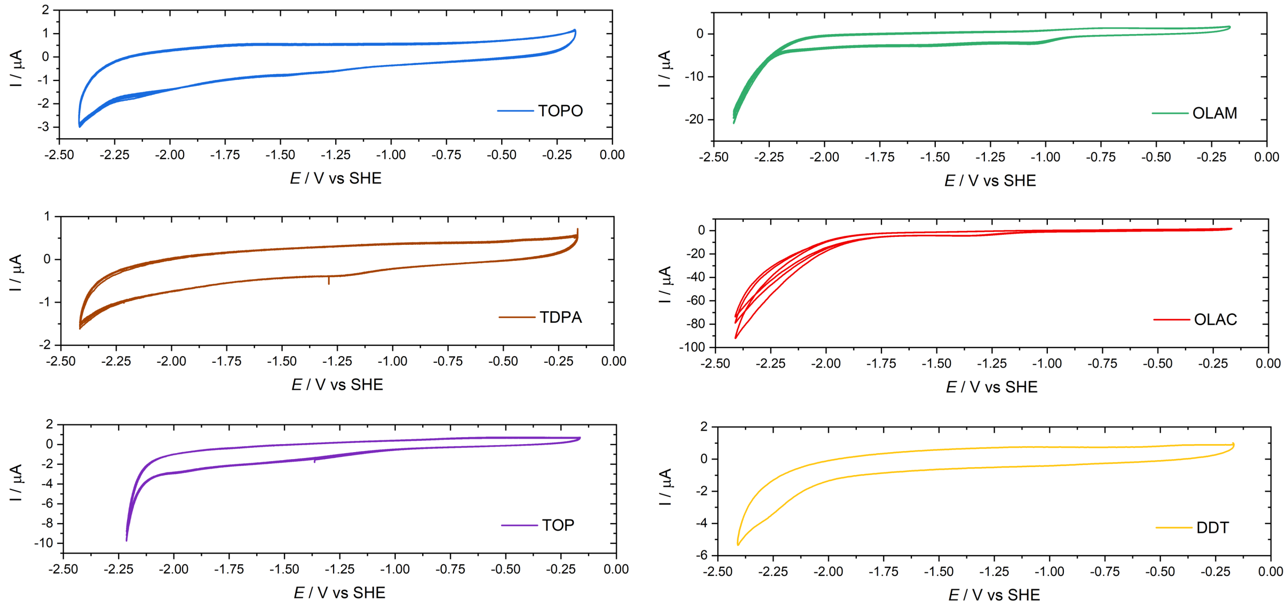

Figure S39. Cyclic voltammograms of free ligands in solution with 0.1 M [^{n}Bu$_4$N][PF$_6$] in MeCN. All of the ligands tested were inactive with respect to electrochemical reduction.

DFT modelling of the metal-ligand interactions

Input geometries were drawn using Avogadro software and consisted of a single Cu atom bonded to the different ligands studied here (OLAM, OLAC, DDT, TOP, TOPO, TDPA). Hydrocarbon chains were all simplified to methyl groups. All further calculations were carried out using Gaussian09. Geometries were all optimised to minimum-energy structures, with no imaginary frequencies, using the B3PW91 functional and 6-31+G(d,p) basis set. Single-point energy calculations were then carried out using the B3PW91/6-311+G(d,p) combination. For these latter calculations, an empirical dispersion correction was also applied (GD3BJ) and water was simulated using the polarizable continuum model.

To estimate the metal-ligand bond strengths, these model ‘complexes’ were fragmented into the Cu atom and frozen ligands (*i.e.* no further geometry optimisation was carried out on the ligands), and the respective single-point energies were calculated for each. The bond energies were then calculated from Equation S7.

Equation S7

$$E_{\mathrm{BOND}} = E_{\mathrm{CuL}} - E_{\mathrm{Cu}} - E_{\mathrm{L}}$$

Table S3. Energies of model Cu-ligand 'complexes' (E_{CuL}), the free copper atom (E_{Cu}), free ligands (E_L), and the calculated bond energies (E_{BOND}) in both atomic units (a.u.) and kcal mol^{-1}. All energies were calculated using the B3PW91 functional, 6-311+G(d,p) basis set, GD3BJ dispersion correction, and water as the solvent.

	E_{CuL} / a.u.	E_{Cu} / a.u.	E_L / a.u.	E_{BOND} / a.u.	E_{BOND} / kcal mol^{-1}
CuTOPO	−2176.802364	−1640.427032	−536.356416	−0.0189160	11.87
CuOLAM	−1736.317014	−1640.427032	−95.865123	−0.0248597	15.60
CuTDPA	−2248.205859	−1640.427032	−607.755001	−0.0238258	14.95
CuOLAC	−1869.068485	−1640.427032	−228.616470	−0.0249835	15.68
CuTOP	−2101.549768	−1640.427032	−461.089270	−0.0334670	21.00
CuDDT	−2078.674153	−1640.427032	−438.208278	−0.0388437	24.37

DFT-optimised geometries and their cartesian coordinates

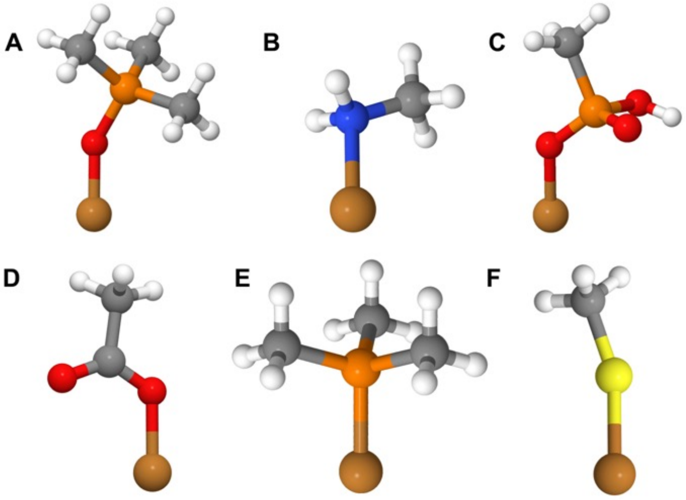

Figure S40. Optimised DFT geometries for the models of: A) **Cu-TOPO**; B) **Cu-OLAM**; C) **Cu-TDPA**; D) **Cu-OLAC**; E) **Cu-TOP**; and (F) **Cu-DDT**.

Cu-TOPO
Charge: 0
Multiplicity: 2
$E = -2176.802364$ a.u.
(Atom X Y Z)

P	-2.24501	0.05286	0.0364
C	-1.92922	-0.90488	1.55146
H	-0.91591	-1.24855	1.55146
H	-2.09529	-0.28406	2.40698
H	-2.5908	-1.7451	1.58667
C	-1.1197	1.48202	-0.02348
H	-0.10637	1.13842	-0.02153
H	-1.30404	2.04401	-0.91516
H	-1.28711	2.10385	0.83104
C	-1.96254	-1.00311	-1.41877
H	-2.15004	-0.44059	-2.30946
H	-0.9487	-1.34522	-1.4198
H	-2.62279	-1.84433	-1.38258
O	-3.86441	0.60208	0.0364
Cu	-4.99624	2.04009	0.0364

Cu-OLAM
Charge: 0
Multiplicity: 2
$E = -1736.317014$ a.u.
(Atom X Y Z)

Cu	-0.9661	-0.07608	0.000
N	0.98257	0.62561	0.000
H	1.08579	1.2276	0.81506
H	1.08583	1.22763	-0.81502
C	2.02349	-0.41998	0.000
H	1.89325	-1.04947	-0.88267
H	3.03993	-0.00911	0.00004
H	1.89319	-1.04953	0.88262

Cu-TDPA
Charge: −1
Multiplicity: 2
$E = -2248.205859$ a.u.
(Atom X Y Z)

Cu	-4.23307	0.73596	0.86446
O	-2.91087	1.79852	0.13502
O	-3.3987	1.14728	2.66131
P	-2.39336	2.00497	1.67331
O	-2.45079	3.66331	2.08652
C	-0.68984	1.38622	1.83936
H	-0.00693	2.11346	1.45252
H	-0.4741	1.20824	2.87217
H	-0.58697	0.47318	1.29103
H	-1.55831	4.01508	2.12307

Cu-OLAC
Charge: −1
Multiplicity: 2
$E = -1869.068485$ a.u.
(Atom X Y Z)

Cu	1.44193	-0.57593	0.000
O	-1.6979	-0.77275	0.000
C	-1.23849	0.37863	0.000
O	0.000	0.72562	0.000
C	-2.2252	1.55446	0.000
H	-3.04584	1.33458	-0.69153
H	-2.66174	1.6569	0.99947
H	-1.74106	2.4907	-0.28842

Cu-TOP
Charge: 0
Multiplicity: 2
$E = -2101.549768$ a.u.
(Atom X Y Z)

Cu	-4.37441	0.60208	0.0364
P	-2.15441	0.60208	0.0364
C	-1.54774	-0.20349	1.55146
H	-0.47774	-0.20349	1.55146
H	-1.90441	0.33109	2.40698
H	-1.90441	-1.21168	1.58667
C	-1.54774	2.31695	-0.02348
H	-0.47775	2.31702	-0.02153
H	-1.90281	2.78995	-0.91516
H	-1.90601	2.85206	0.83104
C	-1.54774	-0.30722	-1.41877
H	-1.90599	0.16527	-2.30946
H	-0.47775	-0.30558	-1.4198
H	-1.90283	-1.31593	-1.38258

Cu-DDT
Charge: −1
Multiplicity: 2
$E = -2078.674153$ a.u.
(Atom X Y Z)

Cu	-4.37441	0.60208	0.0364
S	-2.41942	0.40472	0.98057
C	-1.17358	0.3359	2.25004
H	-0.20428	0.31112	1.79755
H	-1.25332	1.20056	2.87527
H	-1.31424	-0.54534	2.84041

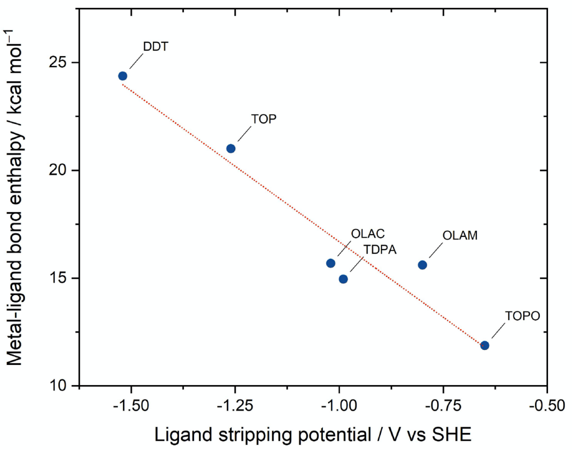

Figure S41. Correlation of the CuNC-ligand binding strength with the SWV ligand-stripping potential

References

[1] N.G. Connelly and W.E. Geiger, *Chem. Rev.*, 1996, **96**, 877–910

[2] D.T. Sawyer, A. Sobkowiak, J.L. Roberts, Electrochemistry for Chemists, 2nd Edition, 1995, p. 192

[3] D. Kim, C.S. Kley, Y. Li, P. Yang, *Proc. Natl. Acad. Sci. U.S.A.* **2017**, *114*, 10560–10565

[4] Z. Hens, J.C. Martins, *Chem. Mater*. **2013**, *25*, 1211–1221

[5] W.T. Osowiecki, J.J. Nussbaum, G. Kamat, G. Katsoukis, M. Ledendecker, H. Frei, A.T. Bell, A.P. Alivisatos, *ACS Appl. Energy Mater*. **2019**, *2*, 7744– 7749

[6] K. Manthiram, Y. Surendranath, A.P. Alivisatos, *J. Am. Chem. Soc*. **2014**, *136*, 7237–7240